Materials Today • Volume xxx, Number xx • xxxx 2021 RESEARCH

ELSEVIER

Lead-free halide double perovskites: Toward stable and sustainable optoelectronic devices

RESEARCH: Review

Asia Bibi [1,†], Ilgeum Lee [1,†], Yoonseo Nah [2,†], Omar Allam [3,4,†], Heejun Kim [1], Li Na Quan [5], Jiang Tang [6], Aron Walsh [7,8,*], Seung Soon Jang [4,*], Edward H. Sargent [9,*], Dong Ha Kim [1,2,*]

[1] Department of Chemistry and Nano Science, Division of Molecular and Life Sciences, College of Natural Sciences, Ewha Womans University, 52, Ewhayeodae-gil, Seodaemun-gu, Seoul 03760, Republic of Korea
[2] Division of Chemical Engineering and Materials Science, College of Engineering, Ewha Womans University, 52 Ewhayeodae-gil, Seodaemun-gu, Seoul 03760, Republic of Korea
[3] The George W. Woodruff School of Mechanical Engineering, Georgia Institute of Technology, 801 Ferst Drive, Atlanta, GA 30332-0405, USA
[4] School of Materials Science and Engineering, Georgia Institute of Technology, 771 Ferst Drive, Atlanta, GA 30332-0245, USA
[5] Department of Chemistry, University of California, Berkeley, CA 94720, USA
[6] Wuhan National Laboratory for Optoelectronics, and School of Optical and Electronic Information, Huazhong University of Science and Technology, Wuhan 430074, Hubei, PR China
[7] Department of Materials, Imperial College London, London SW7 2AZ, UK
[8] Department of Materials Science and Engineering, Yonsei University, Seoul 03722, Republic of Korea
[9] Department of Electrical and Computer Engineering, University of Toronto, 10 King's College Road, Toronto, Ontario M5S 3G4, Canada

In recent years, metal halide perovskites (MHPs) have attracted attention as semiconductors that achieve desirable properties for optoelectronic devices. However, two challenges—instability and the regulated nature of Pb —remain to be addressed with commercial applications. The development of Pb-free halide double perovskite (HDP) materials has gained interest and attention as a result. This family offers potential in the field of optoelectronic devices through flexible material designs and compositional adjustments. We highlight recent progress and development in halide double perovskites and encompass the synthesis, optoelectronic properties, and engineering of the electronic structures of these materials along with their applications in optoelectronic devices. Computational and data-driven statistical methods can also be used to explore mechanisms and discover promising candidate double perovskites.

Introduction

Recently, significant attention has been dedicated to metal halide perovskite (MHP)-based optoelectronic devices, such as solar cells, photodetectors, and light-emitting diodes (LEDs), owing to their impressive optical properties, electrical performance, and solution-processability [1–10]. The perovskite family includes materials with the general formula of ABX_3, as in $CaTiO_3$ [11,12]. The field of perovskite photovoltaics (PVs) has progressed since the first report of MHP-sensitized solar cells using 3D methylammonium lead halide ($MAPbX_3$; where X = I, Br) in 2009 by Kojima et al. [13], which reported solar power conversion efficiencies (PCEs) of 3.13 and 3.81% from $MAPbBr_3$ and $MAPbI_3$, respectively. The performance was further improved in 2012 when Kim et al. [14] reported an MHP-sensitized solid-state solar cell with a PCE exceeding 9%. To date, continuous efforts on device structure optimizations [15–18], interface modifications [18–33], tailoring active layer composition [34–39], morphology control [40–49], and fabrication techniques

* Corresponding authors.
E-mail addresses: Walsh, A. (a.walsh@imperial.ac.uk), Walsh, A. (ted.sargent@utoronto.ca), Jang, S.S. (SeungSoon.Jang@mse.gatech.edu), Kim, D.H. (dhkim@ewha.ac.kr).
† The authors contributed equally to this work.

1369-7021/© 2020 Published by Elsevier Ltd. https://doi.org/10.1016/j.mattod.2020.11.026

Please cite this article in press as: A. Bibi et al., Materials Today, (2021), https://doi.org/10.1016/j.mattod.2020.11.026

[50–53] have led to a promising PCE of more than 23% [54], while the predicted theoretical PCE for MHPs is 31.4% [55,56]. This remarkable PCE of MHPs makes them functionally comparable to polycrystalline silicon and CdTe solar cells [57–60] and as promising candidates for the coming generation of renewable energy. In addition to the rapid development of MHPs in energy applications, these materials have been alternatively used in applications of photodetectors [61–68] and light emitters [69–72]. Although MHP-based optoelectronic devices have been extensively explored for developing real-life applications, they are still far from commercialization due to two fundamental obstacles: (1) the poor structural stability to external environments such as light [73–75], humidity [76–79], oxygen [80,81], temperature or thermal stress [82,83], and electric fields [84–86] and (2) the intrinsic toxicity caused by heavy metals such as lead (Pb) [87,88].

Concerning the stability issue from the device perspective, encapsulation has been the most common strategy [89,90]. Based on material composition, approaches such as changing the organic cation with inorganic counterparts [91,92], using mixed cations and mixed halides [93,94], using low dimensional MHPs (e.g., 2D, 1D, and 0D) [95–101], and forming 2D/3D heterojunction [102–106] have been examined to develop optoelectronic devices with better stability. However, the use of mixed cations or mixed halides induced severe hysteresis problems [13,107,108]. Moreover, the overall device performance using low dimensional MHPs was still far below that of their 3D counterparts. In addition, an attempt to replace toxic Pb with environmentally-friendly alkaline earth metals resulted in higher bandgap materials with compromising optical absorption [109,110]. Substitution with tin (Sn) and germanium (Ge) also led to poor device performance [111–120] in comparison to Pb-based MHPs, due to their ease in oxidation (from 2+ to 4+ oxidation state) [118,121–123]. All efforts concerning an isovalent elemental replacement for $MAPbI_3$ can compromise the desirable optoelectronic properties of conventional 3D MHPs ($MAPbI_3$), which appears impractical for long-term functional optoelectronic applications. Therefore, it is essential to identify an alternative class of materials to overcome the issues of stability and regulation for lead while still maintaining the desirable optoelectronic properties comparable to those of the Pb-based MHPs.

An alternative class of materials has been derived by simply substituting B-site with trivalent metal cations (such as Sb^{3+} and Bi^{3+}) as effective candidates, producing Pb-free HPs with a general formula of $A_3B_2X_9$ [124,125]. Harikesh et al. [126], Park et al. [124] and Zhang et al. [127] used $Rb_3Sb_2I_9$, $Cs_3Bi_2I_9$, and $(MA)_3Bi_2I_9$, respectively, as light harvesters for building solar cells, with PCEs of 0.66, 1.0, and 1.64%, respectively. The poor performance was attributed to their dimensional structures and large bandgap energies [128]. Consequently, $A_3B_2X_9$ perovskites were not considered viable as replacements for Pb-based MHPs.

Heterovalent elemental substitution at the B-site in ABX_3 is another approach toward Pb-free halide perovskite materials, which was first suggested by Volonakis et al. [129] in 2016. In their study, by substituting Pb^{2+} with a pair of non-toxic B^+/B^{3+} cations, they discovered the formation of the "halide double perovskite (HDP)." This perovskite family, based on the elpasolite mineral K_2NaAlF_6, has the general formula of $A_2B^IB^{III}X_6$ with various possible combinations of B^+/B^{3+} and X^- site, such as Cs_2AgBiX_6 (X = Br, Cl) [130–133], $Cs_2AgInCl_6$ [134,135], $Cs_2InSbCl_6$ ($Cs_2InBiCl_6$) [136] and $Rb_2CuInCl_6$ ($Rb_2AgInBr_6$) [137]. These combinations have been extensively studied in recent years. The spectroscopic maximum efficiency (SLME) calculations, based on the integrated optical absorption in the visible range suggested an efficiency of less than 8% for one of the widely studied materials of this class ($Cs_2AgBiBr_6$) [138]. In contrast, higher efficiencies have been predicted for other HDPs with suitable bandgap energies, making them suitable for optoelectronic devices [137]. In an attempt to stabilize Sn-based perovskites, the derivatives with the general formula A_2SnX_6 (such as Cs_2SnX_6, where X = Cl, Br, I) were also reported in which Sn is stable with the 4+ oxidation state. This approach led to air- and moisture-stable compounds referred to as "vacancy ordered double perovskites" and represented as $Cs_2Sn\square X_6$ (where □ is termed a structural vacancy) [139–142].

In this review, starting from their crystal structures, we summarize attractive merits and some demerits of HDPs based on their structural composition along with the systematic studies of electronic structures (Fig. 1). We then present recent developments of this class of materials regarding potential applications in environmentally-friendly optoelectronic devices with superior stability, as depicted in Fig. 2. Computational and statistical approaches are also introduced that provide guidance for the fundamental research and material discovery. Finally, we summarize the challenges and future prospects of this new class of materials by assessing their suitability as a potential alternative to Pb-based perovskites.

Structure of halide double perovskites

The crystal structure of an ideal HDP with the general formula $A_2B_2X_6$ is similar to that of the ABX_3 cubic perovskite archetype. While moving from $AB^{II}X_3$ to $A_2B^IB^{III}X_6$, each B-site cation is substituted by a pair of B^+/B^{3+} cations [143]. HDPs generally consist of two split B-cations in ABX_3 (B^IX_6 and $B^{III}X_6$) and thus form a network structure consisting of alternating B^IX_6 and $B^{III}X_6$ octahedrons with the same A-site cation (e.g., Cs^+) occupying the center of the cuboctahedral cavity [129,132,143,144]. This alternating arrangement of an octahedron of B^IX_6 and $B^{III}X_6$ in a 3D network is termed rock-salt ordering [145]. The crystallographic aspects of HDP were investigated using powder X-ray diffraction (XRD) [146,147] and single-crystal XRD [148]. HDP occupies a cubic face-centered structure with space group Fm-3m [129,132,149] with lattice parameters in a range of approximately 10–12 Å [144]. Structurally, HDP is similar to oxide double perovskites [150] (Sr_2FeMoO_6), which have been comprehensively studied for their unique properties, such as superconductivity, ferromagnetism, and ferroelectricity [151]. In oxide double perovskites, there is clear evidence for order–disorder transitions in the distribution of the two B-site cations depending on the processing conditions [152], and this behavior has also been predicted [138] and observed [153] for some HDPs.

Giustino et al. [154] in 2016 reported that by simply varying the candidate elements that can occupy A, B^I, B^{III}, and X-site,

Please cite this article in press as: A. Bibi et al., Materials Today, (2021), https://doi.org/10.1016/j.mattod.2020.11.026

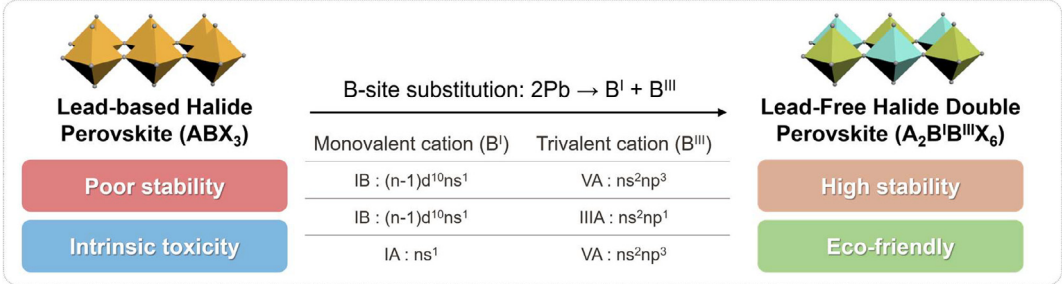

FIGURE 1

Chemical compositions and features of halide double perovskite (HDP) $A_2B^IB^{III}X_6$. By exchanging toxic Pb atoms into non-toxic B^+/B^{3+} elements, three classes of HDPs can be designed for optoelectronic materials.

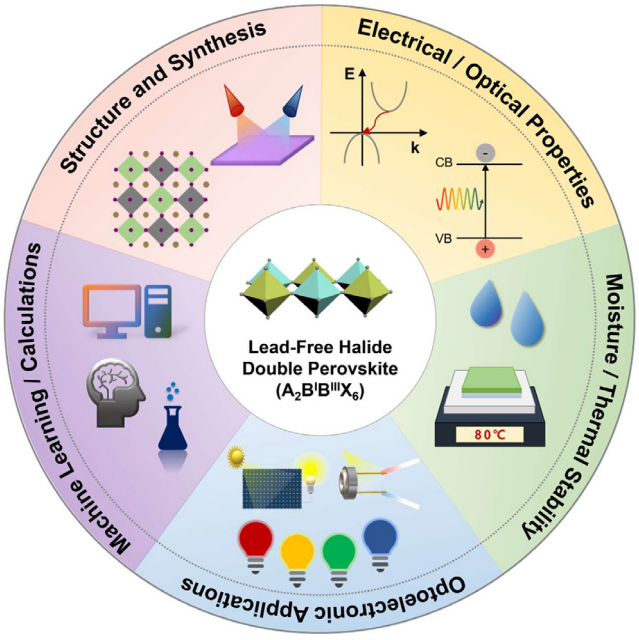

FIGURE 2

Scope of the review toward optoelectronic applications of Pb-free halide double perovskites (HDPs).

9520 possible combinations could be produced. However, for the structural stability of these compounds, two basic but critical criteria must be satisfied: Goldschmidt's tolerance factor (t) and the octahedral factor (μ) [155–158]. The formation of perovskite materials generally occurs when Goldschmidt's tolerance factor and the octahedral factor are in the ranges $0.81 \leq t \leq 1.0$ and $0.44 \leq \mu \leq 0.9$, respectively [159,160]. For $(MA)_2AgBiI_6$, t and μ are 0.86 and 0.5, respectively [156], which are within the range and are also close to those of $MAPbI_3$. Out of 9520 combinations, 900 compounds were stable after applying the selection rule [154]. Moreover, out of 900 compounds, more than 600 compounds have not been investigated yet [154]. The computational screening of these 600 compounds seems demanding; however, this is accessible with modern computational capabilities [136,149,156,161–164]. Machine learning (ML) and first-principle density functional theory (DFT) calculations have also been used to assess the chemical stability of HDPs including disproportionation into secondary phases [64,165,166]. The stability trends predicted by these theoretical approaches are generally in good agreement with experimental findings.

Synthesis protocol for halide double perovskites

The synthetic strategy for preparing stable HDPs as promising PV absorbers involves experimental validations and computational studies [162,167]. As depicted in Fig. 3, the synthesis of HDPs commonly follows: (1) the hydrothermal method [168,169], (2) recrystallization [130] and (3) the solution deposition approach [170]. These pioneering approaches were reported almost simultaneously in 2016 by Slavney et al. [144], McClure et al. [132] and Volonakis et al. [129]. Volonakis et al. [129] prepared Cs_2AgBiX_6 by mixing halide precursors in a stoichiometric ratio and subjected them to a ramping temperature for 5 h, followed by an additional 4 h of heating at 500 °C. McClure et al. [132] followed heat treatment at 210 °C for 10 h to prepare polycrystalline $Cs_2AgBi(Cl/Br)_6$, precipitated from a solution mixture of Ag(Cl/Br), $Bi(Cl/Br)_3$, and Cs(Cl/Br) in a mixed solvent of hydrohalic acid (HCl and HBr) and hydrophosphoric acid (HPA). In contrast, Slavney et al. [144] grew a moisture-stable single crystal of $Cs_2AgBiBr_6$ from halide precursors in HBr solvent, followed by heat treatment at 110 °C.

The hydrothermal approaches proceeded at relatively low temperature and this favored the formation of an ordered structure. However, the presence of impurity peaks, additional phases and a smeared transition at T_c was observed in the reported double perovskite. Moreover, the possibility of mixing A-site-ordered and disordered phase cannot be discounted in the perovskite structure. Thus, many researches have been promoted to further develop highly crystalline and high quality of double perovskite materials [171]. Creutz et al. [172] synthesized colloidal nanocrystals (NCs) of Cs_2AgBiX_6 by rapid injection of trimethylsilyl halide (TMS-X) into a second hot solution composed of silver acetate, bismuth acetate, cesium oleate, oleylamine, and oleic acid in 1-octadecene. The researchers successfully conducted a post-synthesis anion exchange of NCs using TMS-X to tune the halide compositions. Furthermore, Zhou et al. [173] and Bekenstein et al. [174] used slightly different precursors (i.e., $BiBr_3$, $AgNO_3$, and cesium oleate in a 1:1:2 molar ratio) with small amounts of HBr in a high boiling organic solvent. Cesium oleate was injected at a high temperature of 200 °C to obtain colloidal NCs of $Cs_2AgBiBr_6$. Furthermore, the quality of the resulting NCs was improved by controlling the

Please cite this article in press as: A. Bibi et al., Materials Today, (2021), https://doi.org/10.1016/j.mattod.2020.11.026

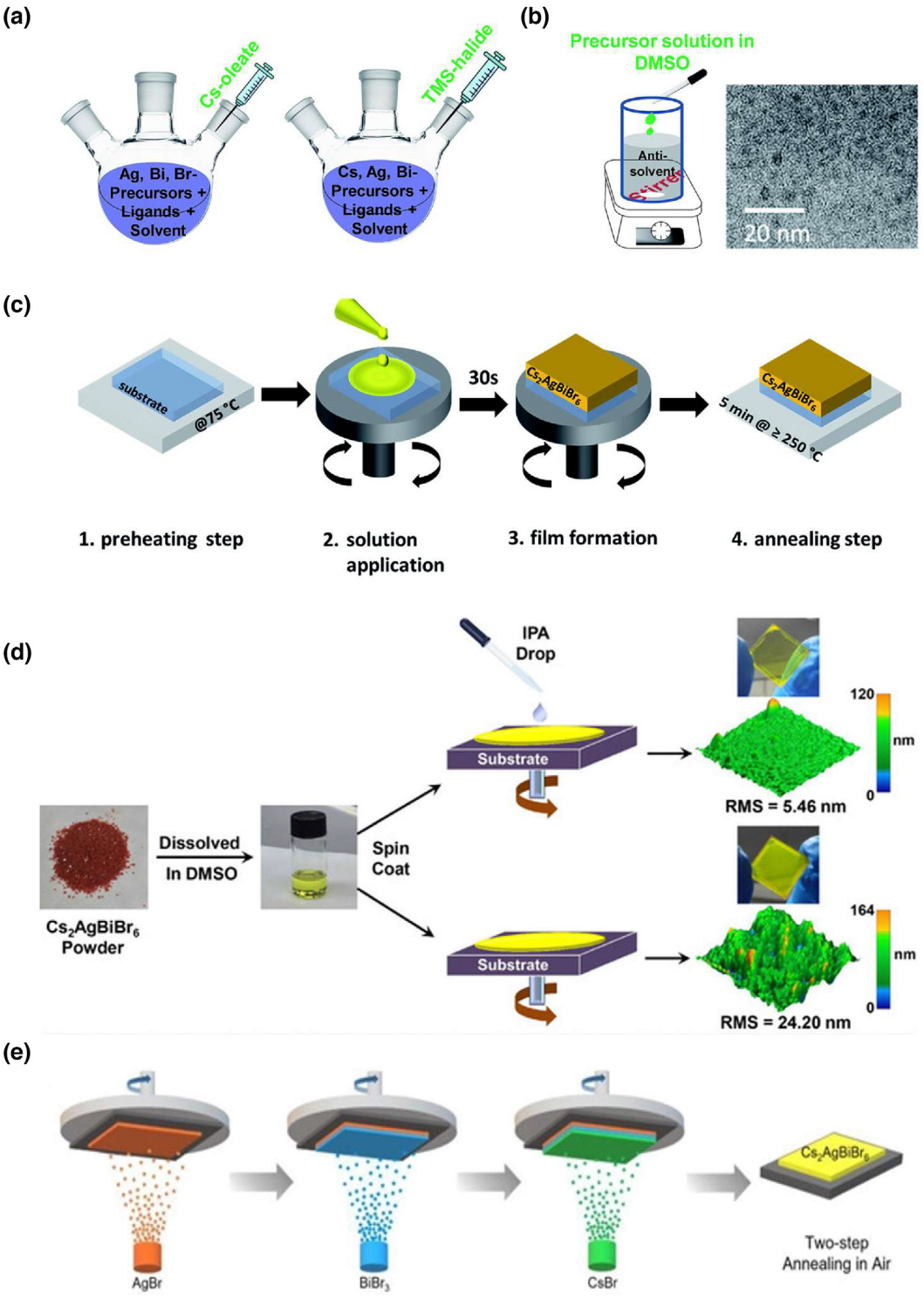

FIGURE 3

Preparations of $Cs_2AgBiBr_6$. (a) Solution phase synthesis of $Cs_2AgBiBr_6$ NCs (hot-injection route). Reproduced with permission [130]. Copyright 2018, Royal Society of Chemistry. (b) Re-precipitation method to synthesize $Cs_2AgBiBr_6$ NCs with a representative TEM image. Reproduced with permission [130]. Copyright 2018, Royal Society of Chemistry. (c) Preheating treatment of stock solution and precursor. Reproduced with permission [170]. Copyright 2017, Royal Society of Chemistry. (d) Effect of anti-solvent on film morphology. Reproduced with permission [189]. Copyright 2018, Wiley-VCH. (e) Sequential vapor deposition processing. Reproduced with permission [230]. Copyright 2018, Wiley-VCH.

additives (such as HBr, oleylamine, and oleic acid) and the reaction time. By using a hot injection approach, Wang et al. [169] synthesized Cs_2SnI_6 with phosphine free, inexpensive and non-toxic tin-based precursors. Zhou et al. [175] successfully synthesized $Cs_2AgInCl_6$ by the hydrothermal method using corresponding chloride precursors (Cs, Ag, and In) in a 2:1:1 ratio,

Please cite this article in press as: A. Bibi et al., Materials Today, (2021), https://doi.org/10.1016/j.mattod.2020.11.026

respectively, using HCl as a solvent. Larger crystal sizes were obtained with longer reaction times.

In the second approach, $Cs_2AgBiBr_6$ NCs were obtained using the recrystallization method [130]. The halide precursors were dissolved in dimethyl sulfoxide (DMSO, considered as an effective solvent), followed by the addition of an anti-solvent such as isopropanol (considered as an ineffective solvent) under vigorous stirring to yield NCs and then separated by centrifugation. This approach resulted in the formation of quasi-spherical NCs, in contrast to those obtained from the previous approaches. The exact reason for the different NC shapes is still unclear, yet similar phenomena have been observed for $CsPbX_3$ NCs [176–178]. In general, different types of interaction between different facets of NCs and organic ligands influences facet energetics and leads to the formation of NCs with minimum energy [179,180]. Several other nanostructures were also synthesized using the recrystallization method. As $CsPbBr_3$ NWs were synthesized by employing the growth time during the recrystallization process [181,182], HDP NWs were synthesized using a similar approach [183,184]. These results implied the potential applications for NW lasers and nanophotonic devices based on HDPs [183–185].

The third approach deposits the precursor solution to obtain high-quality HDP films for device fabrication. Uniform and high-quality crystalline films along with adequate surface coverage are keys to achieving high performance in optoelectronic devices. As a general approach, a $Cs_2AgBiBr_6$ single crystal was prepared, followed by re-dissolution in an organic solvent such as dimethylformamide (DMF) or DMSO [186–188]. In contrast, Greul et al. [170] directly dissolved halide precursors of $Cs_2AgBiBr_6$ in DMSO at 75 °C followed by spin coating of the solution to a preheated substrate and subsequent annealing for greater crystallization. More recently, anti-solvent-assisted crystallization has been reported [189] as an effective approach to obtain a high-quality film with reduced roughness.

The major challenge with preparing HDP is the high processing temperature [129,132,144,170,187,189], which could be as high as 500 °C [129] for solid-state reactions and 110 °C for solution preparation (due to the insolubility of AgCl) [144]. Also, to obtain high-quality crystalline films, the annealing temperature could be as high as 285 °C [170].

For synthesized HDPs phase or compositional purity and preferred orientation was confirmed by XRD pattern [168]. Moreover, phase purity was also assured by temperature dependent PXRD investigations [173]. Whereas, in case of NPs, morphology and size distribution were characterized by transmission electron microscopy (TEM) [169].

Optical and electrical properties of halide double perovskites

Pb-based halide perovskites have remarkable photophysical properties that make them ideal candidates for optoelectronic applications. The optical properties of semiconducting materials are determined by investigating their light-harvesting capacity—absorption coefficients and bandgap energies are calculated for this purpose. Because the absorption threshold is inversely related to the bandgap energy, semiconducting materials with larger bandgaps should have narrow absorption in the visible region. With a bandgap of 1.6 eV at room temperature (RT), $MAPbI_3$ is a direct bandgap semiconductor. Its sharp absorption onset and high absorption coefficient makes it an excellent light absorber. Therefore, transition from ABX_3 to the HDP family requires maintaining the electronic band structure.

In typical 3D MHP ($MAPbX_3$ and $CsPbX_3$), the Pb^{2+} cation (B-site cation) with a valence shell configuration of $6s^26p^0$ [190,191] and a halide ion (X-site anion) dominate the valence and conduction band. Filled Pb $6s^2$ and p^6 orbitals of the halide anion contribute to the formation of the valence band maximum (VBM), while vacant Pb 6p states constitute the conduction band minimum (CBM) [34]. In contrast, MA^+ or Cs^+ cation (A-site cation) affects the tilting and distortion of the PbX_6 octahedron, indirectly influencing the band structure [34]. In an attempt to replace Pb^{2+} with B^+/B^{3+} cation to form HDP, we can obtain the following classes: [143] (1) those with a semi-core d-state, (2) those with a lone pair s-state, and (3) those without an active d-state or s-state. The elements of group IA (Li, Na, K, Rb) and group IB (Cu, Ag, Au) can occupy the B^I-site, and group VA elements (Sb, Bi) can occupy the B^{III}-site. Group IIIA elements (Al, Ga, In, TI) can occupy both the B^I-site and B^{III}-site.

$Cs_2B^I_{(IB)}B^{III}_{(VA)}X_6$ halide double perovskite family [$B^I_{(1B)}$ = Cu, Ag; $B^{III}_{(VA)}$ = Sb, Bi; X = I, Br, Cl]

Ag^+/Bi^{3+} based halide double perovskites

$Cs_2AgBiBr_6$ was the first HDP reported by McClure et al. [132] and Slavney et al. [144] as a potential candidate for PV applications in early 2016. However, $Cs_2AgBiBr_6$ ($Cs_2AgBiCl_6$) exhibited an indirect bandgap of 2.19 eV (2.77 eV) [132], as depicted in Fig. 4(a), (b), (d) and (e). Moreover, mild absorption onset was observed in HDP compared to $MAPbX_3$ perovskites, as depicted in Fig. 4(b) and (c). This late absorption onset confirms that HDP is unsuitable for thin-film PV applications. Nevertheless, such an indirect bandgap favors a long carrier recombination lifetime (~660 ns) [144], as depicted in Fig. 4(f), which is almost two times larger than the recombination lifetime of high-quality $MAPbBr_3$ films (~170 ns) and close to that of $MAPbI_3$ films (~0.736–1 μs) [192]. The electron effective mass and hole effective mass of $Cs_2AgBiCl_6$ ($Cs_2AgBiBr_6$) are 0.53 m_e (0.37 m_e) and 0.15 m_e (0.14 m_e), respectively, which are lighter than their corresponding values for the Pb-based analogs [129,132]. Furthermore, flexibility in variation in the chemical composition of HDP implies facile tuning of the bandgap [154,193,194]. However, the literature includes a wide variation in the calculated bandgap value of Cs_2AgBiX_6 attributed primarily to the difference in preparation methods [132,149,195], as depicted in Table 1. Characterization techniques also influenced the bandgap value [132,144,196].

Because bandgap energy is largely dependent on the lattice parameter, various strategies, including controlling temperature or pressure, doping with other elements, and adjusting the chemical composition, can be used to alter the bandgap from indirect to direct [129,197]. Li et al. [198] demonstrated pressure-dependent bandgap engineering for $Cs_2AgBiBr_6$, as depicted in Fig. 5(a), and claimed an approximately 22.3% reduction of bandgap by high-pressure treatment, therefore attaining a

Please cite this article in press as: A. Bibi et al., Materials Today, (2021), https://doi.org/10.1016/j.mattod.2020.11.026

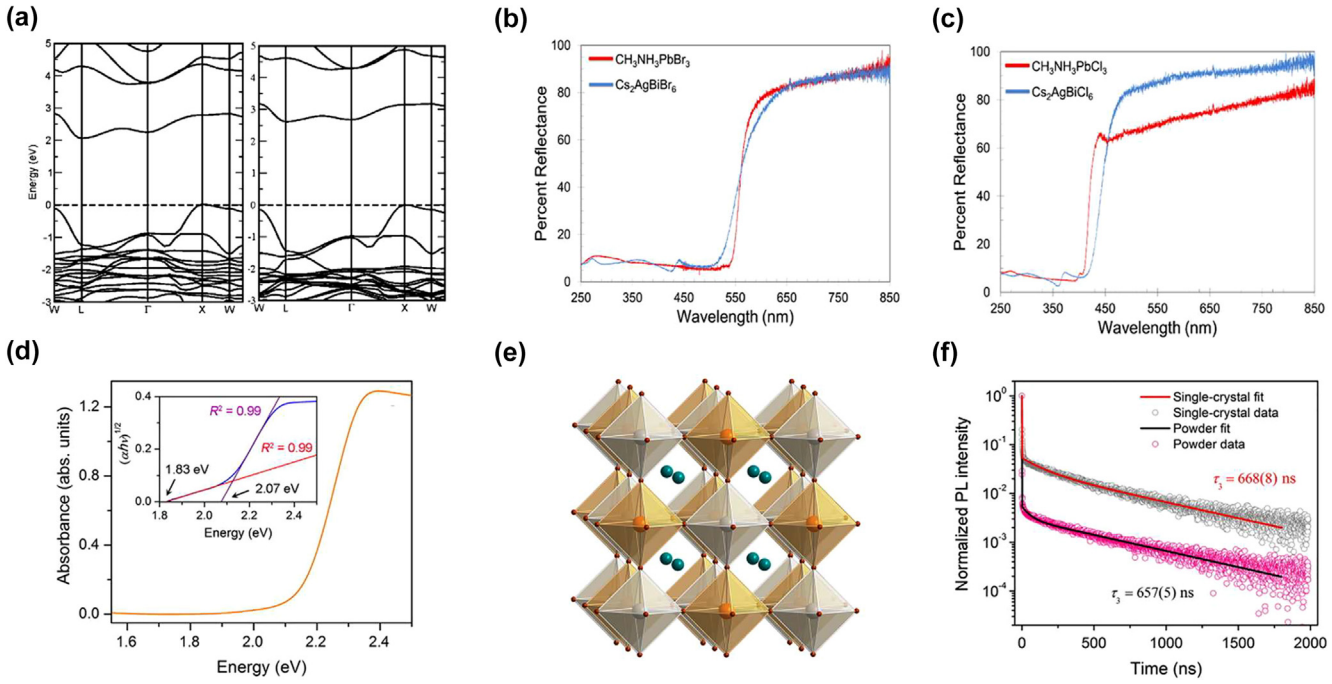

FIGURE 4

Band structure diagrams for (a) $Cs_2AgBiBr_6$ (left), $Cs_2AgBiCl_6$ (right) and UV-Vis diffuse reflectance spectra for (b) $Cs_2AgBiCl_6$ and $MAPbCl_3$ (c) $Cs_2AgBiBr_6$ and MAPbBr3. Reproduced with permission [132]. Copyright 2016, American Chemical Society. (d) Absorbance spectrum of $Cs_2AgBiBr_6$ powder sample with Tauc plot inset. (e) X-ray structure of the ordered double perovskite $Cs_2AgBiBr_6$. Orange, gray, turquoise, and brown spheres represent Bi, Ag, Cs, and Br atoms, respectively. (f) Time-resolved room-temperature PL and fits for the PL decay time (τ) in powder and single-crystal samples. Reproduced with permission [144]. Copyright 2016, American Chemical Society.

bandgap comparable to that of $MAPbI_3$. However, under ambient conditions after releasing pressure, the compound only retained 8.2% reduction of its bandgap value.

Doping is also an effective strategy to alter the bandgaps. Slavney et al. [199] successfully incorporated a very low concentration of thallium (Tl) to obtain $Cs_2Ag_{1-a}Bi_{1-b}Tl_xBr_6$ and selectively modified the band edges of $Cs_2AgBiBr_6$ to engineer a bandgap. Based on theoretical calculations, they demonstrated that Tl doping on the Ag^+-site (Bi^{3+}-site) resulted in a direct (indirect) bandgap with a bandgap reduction of 0.1 eV (0.8 eV), as depicted in Fig. 5(b). Direct evidence for a bandgap reduction was found based on the color change from opaque black to translucent orange, as evident in Fig. 5(d). Moreover, the carrier lifetimes were comparable to that of $MAPbI_3$, demonstrating the potential of this alloyed compound in solar cells. However, Tl is 10 times more toxic than Pb, which restricts the commercial application of this alloyed compound for sustainable optoelectronic devices. Du et al. [200] incorporated In^{3+} and Sb^{3+} in $Cs_2AgBiBr_6$ to obtain substituted HDPs of $Cs_2AgBi_{1-x}In_xBr_6$ and $Cs_2AgBi_{1-x}Sb_xBr_6$, demonstrating a bandgap modulation of ~0.41 eV to address the Tl toxicity issue. However, these compounds were unstable and exhibited a narrow phase diagram region. In contrast, Zhang et al. [197] demonstrated that the bandgap of $Cs_2AgBiBr_6$ could be adjusted from indirect to direct by altering the atomic arrangement of the Ag-Bi lattice, resulting in band hybridization and reduced crystal symmetry leading to a shift in the VBM.

Ag^+/Sb^{3+}-based halide double perovskites

Tran et al. [201] synthesized single crystals of $Cs_2AgSbCl_6$ and $Cs_2AgInCl_6$ with indirect and direct bandgaps, respectively. Moreover, as depicted in Fig. 5(c), the bandgap of the alloyed compound $Cs_2AgSb_xIn_{1-x}Cl_6$ changes from direct to indirect with an increase in Sb content. A single crystal of $Cs_2AgSbCl_6$ has an indirect bandgap, which is temperature-dependent. Recently, Zhou et al. [175] suggested with computational studies that the bandgap can be varied by introducing atomic disorder in the B-cation distribution of $Cs_2AgSbCl_6$.

Volonakis et al. [129] and Zhao et al. [137] proposed Cu-based perovskites as an alternative to Ag-based HDPs. However, no Cu-based three-dimensional HDPs have been synthesized so far. This was explained by Xiao et al. [202] who considered the $3d^{10}$ electronic configuration of Cu^+. The valence orbitals readily hybridize with either the 4 s or 4p to lower the energy. Therefore, Cu^+ is more covalent and tends to favor four-fold coordination environments over the 6-fold octahedral environment found at the perovskite B-site.

$Cs_2B^I_{(IB)}B^{III}_{(IIIA)}X_6$ halide double perovskite family [$B^I_{(1B)}$ = Cu, Ag; $B^{III}_{(IIIA)}$ = Ga, In, Tl; X = I, Br, Cl]

Group-IIIA elements were considered, especially indium (In), to overcome the limitations caused by the indirect bandgap of bismuth-based HDPs. The reason for the growing interest in In^{3+} was its direct bandgap formation in combination with Ag^+ [134]. Tran et al. [201] successfully synthesized a single crystal

Please cite this article in press as: A. Bibi et al., Materials Today, (2021), https://doi.org/10.1016/j.mattod.2020.11.026

TABLE 1

Summary of categories of halide double perovskites (HDPs).

Material	Method of preparation	Optical transitions	Bandgap (eV)	References.
$Cs_2B^{I}_{(IB)}B^{III}_{(VA)}X_6$ halide double perovskite family				
$Cs_2AgBiBr_6$	Solution process	Direct/indirect	2.21/1.95	[144]
		Direct/indirect	2.2/2.4	[228]
	Solution process and solid-state reaction	Direct/indirect	2.51/1.83, 1.97	[149]
		Indirect	2.19, 2.06	[132]
	Solution process and precipitation	Indirect	2.0	[265]
	Vacuum sublimation	Indirect	2.02	[230]
	Two-step spin coating of precursor solution	Indirect	2.02	[196]
$Cs_2AgBiCl_6$	Solid-state reaction and solution process	Indirect	2.77, 2.62	[132]
		Direct/indirect	2.96/2.42, 2.48	[149]
	Solution process and precipitation	Indirect	2.5	[265]
$Cs_2AgSbCl_6$	Hydrothermal method	Direct/indirect	3.33,2.36/2.35,1.4	[173]
	Hydrothermal method and solid-state reaction	Indirect	2.54	[201]
$Cs_4CuSb_2Cl_{12}$	Precipitation reaction	Direct	0.9,1.02	[266]
$Cs_2B^{I}_{(IB)}B^{III}_{(IIIA)}X_6$ halide double perovskite family				
$Cs_2AgInCl_6$	Hydrothermal method	Direct	3.2	[203]
	Hydrothermal method and solid-state reaction	Direct	3.53	[201]
$Cs_2CuInCl_6$	Solid-state synthesis	Direct	1.01	[200]
Vacancy ordered halide double perovskites				
Cs_2SnI_6	Solution Process	Direct	1.26	[140]
	Chemical bath deposition	Direct	1.49	[267]
	Two-step vapor deposition and solid-state reaction	Direct	1.48	[268]
Cs_2SnCl_6	Hydrothermal method	Direct	3.9	[244]
$Cs_2SnI_3Br_3$	Solid-state reaction	Direct	1.43	[142]
Cs_2TiBr_6	Two-step vapor deposition method	Direct	1.82	[233]
Rb_2SnI_6	Solution precipitation	Direct	1.32	[269]
Layered halide double perovskites				
$(BA)_4AgBiBr_8$	Solution process and crystallization	Direct	1.72	[209]
$(BA)_2AgBiBr_7$	Solution process and crystallization	Direct	1.60	[209]
Hybrid halide double perovskites				
$(MA)_2AgBiBr_6$	Hydrothermal method	Indirect	2.02	[224]
$(MA)_2AgBiI_6$	Solid-state reaction	Indirect	1.25, 1.96, 1.02, 1.89	[224]
$(MA)_2AgSbI_6$	Solid-state reaction	Direct	1.93	[222]
$(MA)_2KBiCl_6$	Hydrothermal method	Direct/indirect	3.37, 3.15/3.04, 3.02	[227]
$(MA)_2TlBiBr_6$	Hydrothermal method	Direct	2.16	[270]

of $Cs_2AgInCl_6$ with a direct bandgap. Subsequently, Volonakis et al. [134] reported that $Cs_2InAgCl_6$, with an altered atomic arrangement, has a direct bandgap of 3.3 eV. Unfortunately, the absorption coefficient was much smaller throughout the visible region. A single crystal of $Cs_2AgInCl_6$ exhibits both parity-allowed and parity-forbidden transitions [203], as depicted in Fig. 6(a). The room temperature time-resolved photoluminescence (PL) spectra demonstrated that the PL-lifetime of parity-allowed transitions was shorter than that of parity-forbidden transitions. The absorption coefficient was weak because of parity-forbidden transitions, making them unsuitable for thin-film PV applications. Recently, Nag et al. [204] introduced lattice doping as an attempt to improve the optical functionality of $Cs_2AgInCl_6$. Through the manganese ion (Mn^{2+}) doping, visible PL-intensity was enhanced, as depicted in Fig. 6(b), because $Cs_2AgInCl_6$ absorbs ultraviolet (UV) light and transfers the excitation energy to d-electrons of Mn^{2+}.

As previously described, defects influence material properties such as carrier mobility, diffusion length, and non-radiative recombination rates. Based on DFT calculations, Xu et al. [205] suggested that growing n-type $Cs_2AgInBr_6$ without unwanted phases requires conditions that are Ag^+-rich and Br^--poor. In contrast, Li et al. [206] proposed In^{3+}-poor and Cl^--rich conditions to obtain shallow defects in $Cs_2AgInCl_6$. Unfortunately, $Cs_2AgInBr_6$ preparation is not energetically favored.

In another attempt to achieve a direct, narrow bandgap with In^{3+}-based HDPs, Ag^+ was replaced with Cu^+ (e.g., $Cs_2CuInCl_6$), and many theoretical studies were supported [137,163,164,175]. The superior electronic band structure in $Cs_2CuInCl_6$ can be attributed to Cu d^{10} states, which form antibonding hybridization with the halide p-state. However, DFT calculations reveal that Cu^+-based HDPs are energetically unfavorable compared to Ag^+ analogs [202]. Not surprisingly, this compound has not been synthesized experimentally so far.

$Cs_2B^{I}_{(IA)}B^{III}_{(VA)}X_6$ halide double perovskite family [$B^{I}_{(1A)}$ = Li, Na, K, Rb; $B^{III}_{(VA)}$ = Sb, Bi; X = I, Br, Cl]

In contrast to several members in $A_2B^{I}_{(IB)}B^{III}_{(VA)}X_6$, this $Cs_2B^{I}_{(IA)}B^{III}_{(VA)}X_6$ HDP family is thermodynamically stable but possesses indirect and large bandgaps, which make them unsuitable for thin-film PV applications. Sodium-based perovskites, such as Cs_2NaSbI_6 and Cs_2NaBiI_6, possess optical bandgaps of 2.03 and

Please cite this article in press as: A. Bibi et al., Materials Today, (2021), https://doi.org/10.1016/j.mattod.2020.11.026

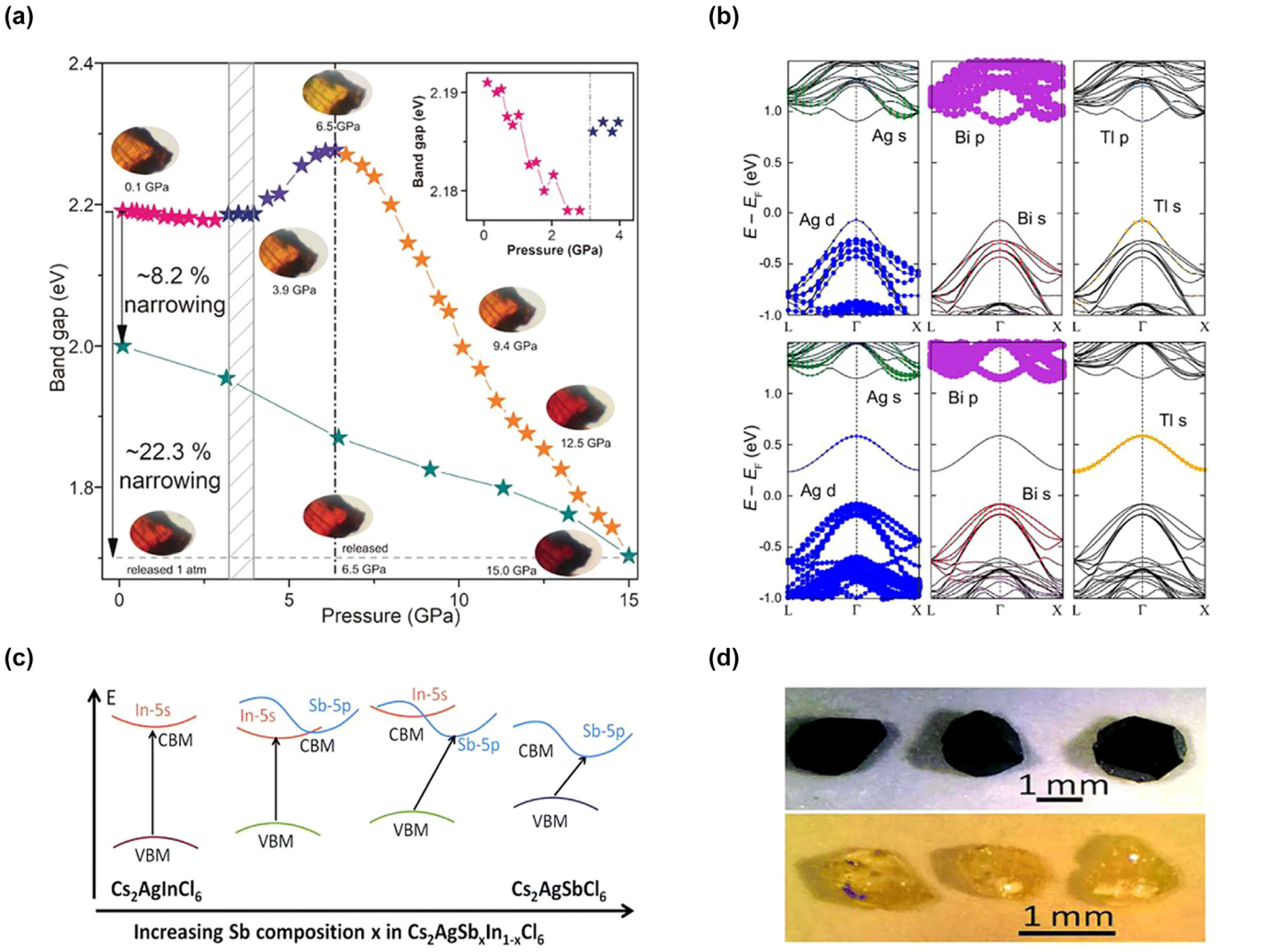

FIGURE 5

(a) Bandgap evolution of the $Cs_2AgBiBr_6$ crystal at high pressure and representative optical micrographs of piezo-chromic transitions. Reproduced with permission [198]. Copyright 2017, Wiley-VCH. (b) Band structures of $Cs_2(Ag_{1-a}Bi_{1-b})Tl_xBr_6$ for (top) substitution of Tl^+ for Ag^+ and (bottom) substitution of Tl^{3+} for Bi^{3+}. Metal orbital characters of the bands are depicted in color. Reproduced with permission [199]. Copyright 2017, American Chemical Society. (c) A change in the character of the CBM from s-orbital-derived to p-orbital. (d) Single crystals of double perovskites $Cs_2AgSbCl_6$ (top) and $Cs_2AgInCl_6$ (bottom), respectively. Reproduced with permission [201]. Copyright 2017, Royal Society of Chemistry.

2.43 eV, respectively [164]. As depicted in Fig. 6(c), both iodide compounds and $Cs_2NaSbBr_6$ exhibit absorption in the visible region, attributed to p-p valence to conduction band transitions. Zhao et al. [164] predicted a bandgap dependence of $Cs_2NaB^{III}X_6$ on the B^{III}-site cation and X-site halide ion. The bandgap would be narrower with (1) a large size anion and (2) Sb^{3+} (B^{III}-site) cation. Zhang et al. [207] also demonstrated the empirical information of Cs_2NaBiI_6 with a bandgap energy of 1.66 eV, which is comparable to that of $MAPbI_3$; however, the low film quality produced poor device performance.

Recently, in an attempt to alter the electronic properties based on the degree of cation order, the band structure of $Cs_2NaSbCl_6$ was studied with different Na^+/Sb^{3+} cation distributions [197]. As depicted in Fig. 6(d), six different distributions of Na^+/Sb^{3+} were considered; only Configuration 6 (C6) corresponded to the ordered (with only nearest Na-Sb bond) $Cs_2NaSbCl_6$ compound with an indirect bandgap, whereas the other 5 configurations corresponded to a disordered (with some Sb-Sb bonds) $Cs_2NaSbCl_6$ structure with direct bandgaps. Moreover, bandgaps decreased monotonously from C6 to C1 owing to greater Sb^{3+} cation density (more Sb-Sb bonds). The calculated optical absorption coefficient also improved for disordered compounds as their absorption onset moved toward lower energies, which was consistent with the calculated band structure.

Layered halide double perovskites

High electronic dimensionality is another important criterion for promising solar-absorbing candidates [206]. Accordingly, Tang et al. [208] designed a layered HDP with the general formula $Cs_{3+n}B_nSb_2X_{9+3n}$ (B = Sb, Ge) by incorporating an octahedral layer of $[BI_6]$ into $Cs_3Sb_2I_9$, as depicted in Fig. 7(a). The resulting layered perovskite exhibited a suitable bandgap, large dielectric constant, smaller carrier effective mass (m_e), high optical absorption, and low exciton binding energies. Moreover, the bandgap of the compound was easily tuned by controlling the number of layers.

Please cite this article in press as: A. Bibi et al., Materials Today, (2021), https://doi.org/10.1016/j.mattod.2020.11.026

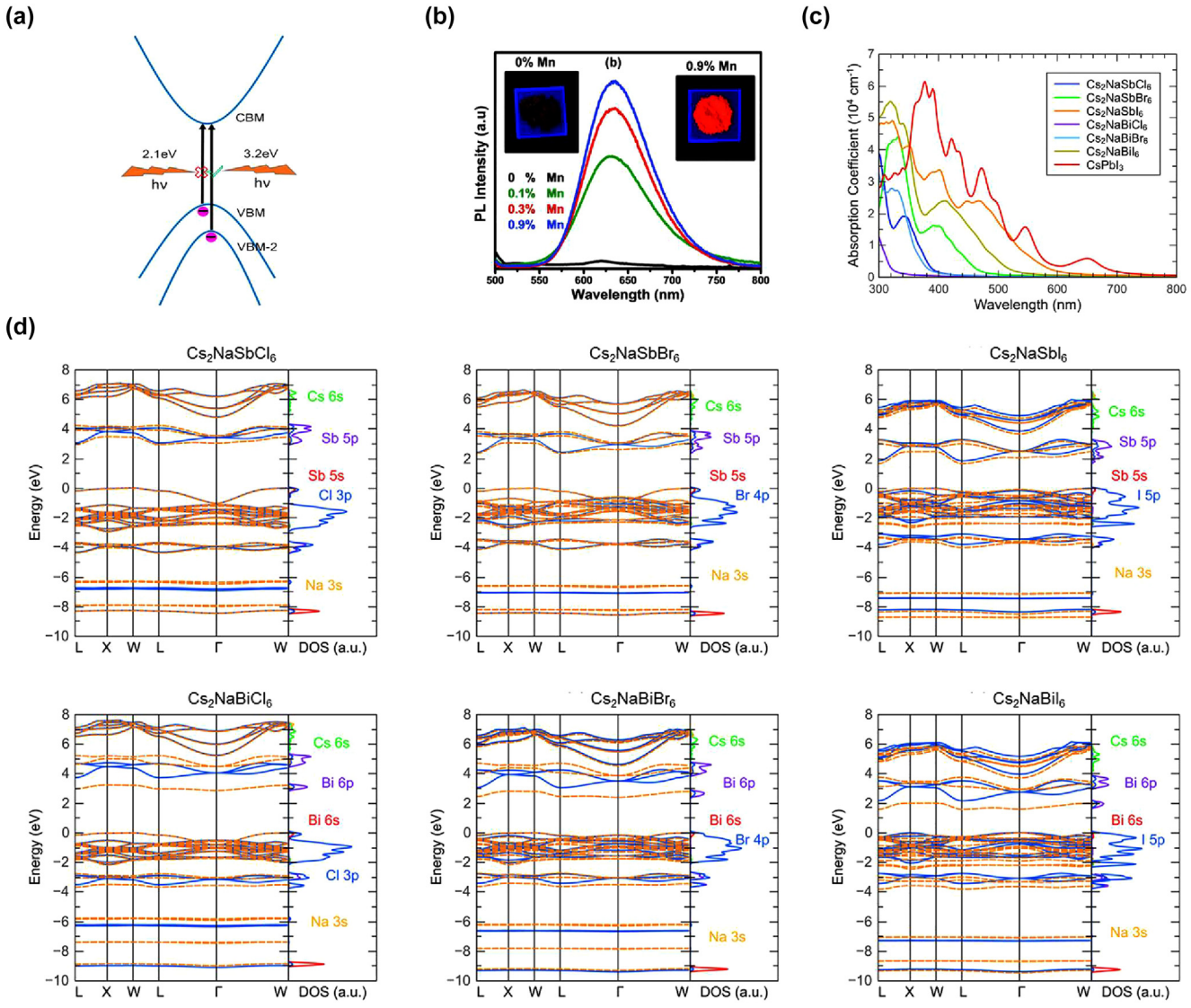

FIGURE 6

(a) Schematic illustration of the parity-forbidden transitions of $Cs_2AgInCl_6$. Reproduced with permission [203]. Copyright 2018, American Chemical Society. (b) PL spectra of Mn-doped $Cs_2AgInCl_6$ with different Mn content after excitation with 340 nm light. Insets illustrate photographs of luminescence from the powder samples under UV light. Reproduced with permission [204]. Copyright 2018, Royal Society of Chemistry. (c) Calculated optical absorption spectrum for the double perovskites of the form Cs_2NaBX_6 compared with $CsPbI_3$. (d) Scalar relativistic (solid blue lines) and fully relativistic (dashed orange lines) band structures and fully relativistic partial density of states (DOS) for the double perovskites. The highest occupied state is set to 0 eV. Reproduced with permission [252]. Copyright 2018, Elsevier Ltd.

In 2018, Connor et al. [209] demonstrated the effect of dimensional confinement on 3D $Cs_2AgBiBr_6$ HDP by synthesizing 2D derivatives using long-chain aliphatic cations (butylammonium cations) such as $(BA)_4AgBiBr_8$ ($n = 1$) and $(BA)_2CsAgBiBr_7$ ($n = 2$). The long-chain cation spacer separated the inorganic sheets while the Cs^+ cation occupied the cavities of inorganic layers, as depicted in Fig. 7(b). Due to the dimensional reduction, the bandgap of the material changed from the indirect to the direct configuration, as depicted by the DFT results in Fig. 7(c). Although electronic structure calculations exhibited direct gap transitions in $(BA)_4AgBiBr_8$, its powder exhibited lower energy-absorption onset than corresponding films.

Summary and outlook

Overall, despite the attractive semiconductor features of HDPs, there are limitations including the indirect bandgap and late absorption onset. Although the optical performance of HDPs has lagged behind Pb-based halide perovskites, HDPs still have potential for the development and more extensive research on fundamental properties of HDPs is required. Further studies on the quantum confinement effect of HDP NCs should also be conducted, as the photophysical properties of NCs are expected to be different from their bulk counterparts. Several researchers have reported blue-shifted excitonic absorption peak, size-dependent spectral shifts and enlarged bandgap as evidence of quantum confinement in HDP NCs [172,210]. However, it remains contro-

Please cite this article in press as: A. Bibi et al., Materials Today, (2021), https://doi.org/10.1016/j.mattod.2020.11.026

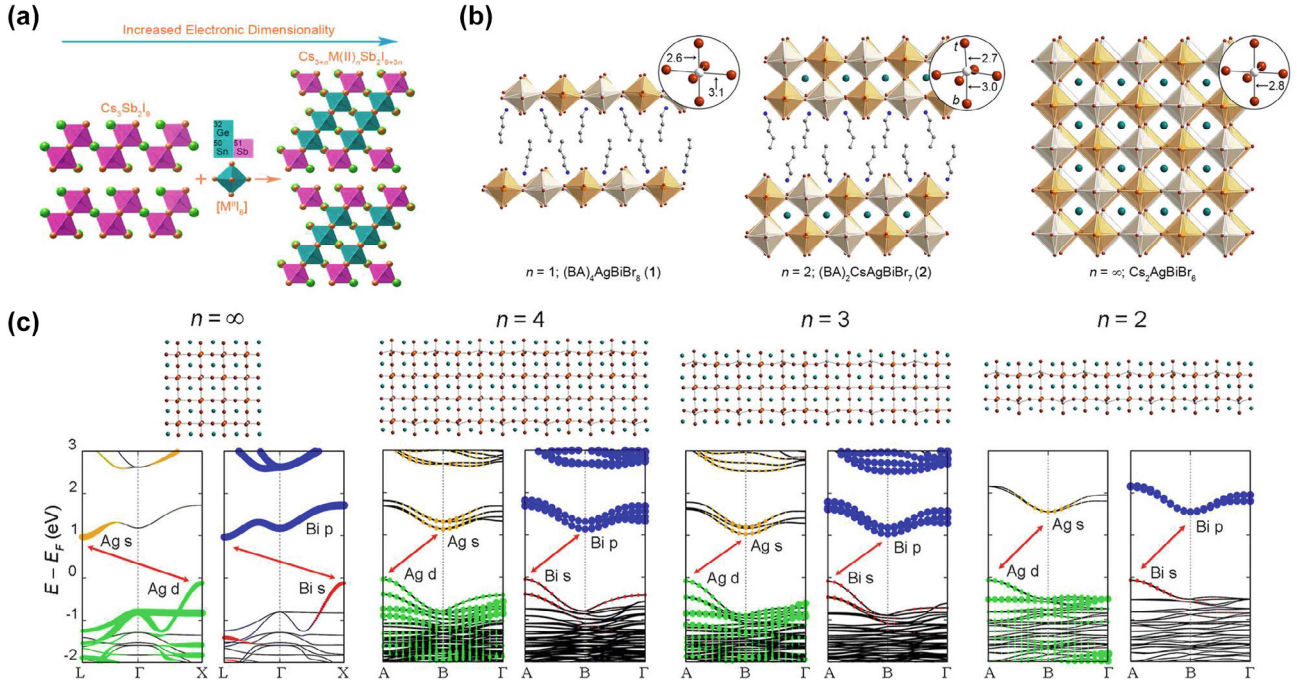

FIGURE 7

(a) Illustration of the general design principle for the layered HDPs $Cs_{3+n}M(II)_nSb_2X_{9+3n}$ (M = Sn, Ge). Cs and I atoms are depicted with green and orange spheres, respectively; Sb and Sn(Ge) atoms displayed in purple and cyan, respectively. Reproduced with permission [208]. Copyright 2018, American Chemical Society. (b) Single-crystal X-ray structures (298 K) of the (001) layered double perovskites $(BA)_4AgBiBr_8$ ($n = 1$) $(BA)_2CsAgBiBr_7$ ($n = 2$), and the 3D double perovskite $Cs_2AgBiBr_6$. Insets illustrate the Ag coordination sphere with select bond distances in Angstroms. (c) Atomic geometries and band structures of $Cs_2AgBiBr_6$ (3D) and model $n = 4$, $n = 3$, and $n = 2$ perovskites. Gray, orange, brown, and teal spheres represent Ag, Bi, Br, and Cs atoms, respectively. The dominant metal orbital character of the bands is depicted in color. Red arrows indicate the lowest-energy transitions. Reproduced with permission [209]. Copyright 2018, American Chemical Society.

versial whether these results are inconsistent due to the differences in measurement techniques [174,211].

It is also noteworthy that structural dimensionality does not necessarily indicate the electronic dimensionality [206]. While the electronic properties of the Pb-based perovskites are primarily determined by the BX_6 octahedra, the electronic landscape of HDPs rely on the lone pair states of two B-site cations. In this regard, three-dimensional (3D) HDPs can exhibit low electronic dimensionality due to the nature of alternating arrangement of B^IX_6 and $B^{III}X_6$ octahedrons in 3D network. Therefore, not only the structural dimension but also the electronic dimension of the absorbing material should be considered for improved PV properties [212].

Moreover, various studies have shown that the refractive index plays a vital role in determining optical response properties of halide perovskites [213] and the relationship between energy gap and refractive index is continuously gaining interest [213–215]. Recently, an elaborative study [216] of Cs_2AgCrX_6 (X = Cl, I) suggested that halogen substitution at the X-site leads to refractive indices (n) value of 2.1, 2.5, and 3.0 for $Cs_2AgCrCl_6$, $Cs_2AgCrBr_6$, and Cs_2AgCrI_6, respectively, while A-site engineering $A_2AgCrBr_6$ (A = K, Rb, Cs) leads to refractive index (n) around 2.5, 2.3, and 2.4 for $Cs_2AgCrBr_6$, $Rb_2AgCrBr_6$, and $K_2AgCrBr_6$, respectively. The n values were found to increase with increase of photon energy in the region 0.0–3.0 eV. On the other hand, refractive indices of $CH_3NH_3PbI_{3-x}Cl_x$ perovskite thin films were reported approximately to be 2.4 and 2.6 in the visible to near-infrared wavelength region. Crystal orientation of organic–inorganic hybrid perovskites has also been well studied for fine tuning of optoelectronic properties [217]. However, this window needs to be still explored for Pb-free HDPs.

Stability of halide double perovskites

As discussed previously, the most critical drawbacks associated with typical $MAPbI_3$ perovskites are their instability to light, moisture, oxygen, and heat, leading to severe degradation to PbI_2. Additionally, toxic lead is still necessary to achieve high performance, even though it causes serious harm to human health such as fatigue, muscle weakness and clumsiness. Thus, extensive efforts have been paid to design new non-/low-toxic and stable halide perovskites for the optoelectronic applications. Sn^{2+} and Ge^{2+} could be expected as alternative candidates to replace with Pb^{2+} ions in the perovskites [218,219]. These non-toxic materials are subject to oxidize due to high-energy-lying 5s orbitals. Afterwards, bivalent metal ions such as Sr^{2+} [218], Co^{2+} [220] and Zn^{2+} [221] were adopted to partially replace the lead to enhance both efficiency and stability. However, the doping method cannot thoroughly solve the issues of stability or toxicity. Recently, HDP have been proposed as stable and green alternatives to lead halide perovskites, and these novel family of perovskite structure may overcome these problems and demonstrate significantly high stability to these weather elements. In this section, the stability were improved by substitut-

Please cite this article in press as: A. Bibi et al., Materials Today, (2021), https://doi.org/10.1016/j.mattod.2020.11.026

ing different elements. The photo- and moisture stability could be improved by investigating of $Cs_2Ag^{I}B^{III}X_6$ (B = Bi, In, Sb), (X = Cl, Br) and the thermal stability were investigated with the structure of $Cs2B^{I}B^{III}X^6$ (B^{I} = Cu, Ag, Au; B^{III} = Bi, Sb; X = Cl, Br, I). These different substitution in the HDP structure exhibited much higher photo, moisture and thermal stability.

Photo- and moisture-stability

Many studies have demonstrated the ambient stability of HDPs. McClure et al. [132] investigated the stability of Cs_2AgBiX_6 (X = Cl, Br) in ambient atmosphere. Samples were stable under dark conditions for two weeks, yet darkening was observed when exposed to visible light. As shown in Fig. 8(a) and (b), $Cs_2AgBiCl_6$ undergoes minimum degradation over 28 days which is confirmed by the slight change in total reflectance, while $Cs_2AgBiBr_6$ illustrates severe degradation. Superior stability of chloride-based HDPs was also observed by Volonakis et al. [134]. $Cs_2AgInCl_6$ was structurally stable for more than three months when exposed to light and moisture. Zhou et al. [175] also demonstrated the crystallographic stability of $Cs_2AgInCl_6$ to light and moisture for more than 28 days.

For $Cs_2AgBiBr_6$ NCs, Zhou et al. [168] demonstrated phase uniformity for 90 days under 55% relative humidity; the material could withstand a light soaking of 70 $mWcm^{-2}$ for 500 h. Slavney et al. [144,199] also investigated the stability of freshly-prepared $Cs_2AgBiBr_6$ powder by exposing it to light and moisture. As depicted by the XRD pattern in Fig. 8(c), the material exhibited stability in dark ambient conditions even after 30 days. However, severe discoloration was observed within 15 days of exposure to light, which was attributed to the photosensitivity of Ag salts. Similar phenomena have been reported for other Ag-based HDPs, such as $Cs_2AgInBr_6$, $Cs_2AgBiCl_6$, and $Cs_2AgSbCl_6$ [132,173]. In the case of hybrid HDPs, $(MA)_2AgBiI_6$ did not decompose even after four months of storage under dark humid conditions, and $(MA)_2AgSbI_6$ was stable under ambient conditions for 370 days [222].

Thermal stability

Assessment of the inherent stability of HDPs is critical for their commercialization. Filip et al. [34,149,163] theoretically demonstrated thermodynamic stabilities of $Cs_2B^{I}B^{III}X_6$ (B^{I} = Cu, Ag, Au; B^{III} = Bi, Sb; X = Cl, Br, I) and suggested that only 3 were stable among 18 hypothetical compounds. Dong et al. [223] and Wei et al. [224] also conducted a study on the thermal stability of $Cs_2AgBiBr_6$ and $(MA)_2AgBiBr_6$ in comparison to $CsPbBr_3$ and $MAPbI_3$, respectively. Based on the experimental values, it was found that $Cs_2AgBiBr_6$ possessed superior stability which was attributed to the strong metal-halide bonding and the absence of organic components. $Cs_2AgBiBr_6$ maintained its phase purity for several months [196,225]. However, thermodynamic stability decreased as X-site halide ion changed from Cl^- to I^- [136,161,163,165]. $Cs_2AgInCl_6$ also exhibited thermal stability up to 400 °C with any change in phase and mass [175]. In another study, the same compound was stable for three months [226]. However, Xu et al. [226] demonstrated that point defects of $Cs_2AgInCl_6$ have low formation energy. These defects can be suppressed by altering the growth conditions (Bi/In poor and halogen rich), but their presence affects the electronic band structure and thus leads to poor photophysical properties.

For hybrid HDPs (MA^+ or FA^+ as A-site cation), thermal stability is lower than that of all-inorganic HDPs due to the presence of organic cations, as shown in Fig. 8(d). However, these compounds are significantly more stable than Pb-based hybrid perovskites such as $MAPbX_3$ [227]. A thermal gravimetric analysis (TGA) of $(MA)_2AgBiBr_6$ confirmed thermal stability of up to ~550 K with a heating rate of 10 K min^{-1}. Antimony-based hybrid double halide perovskites $(MA)_2AgSbI_6$ [222] were also stable for 370 days under ambient conditions.

Optoelectronic applications of halide double perovskites

Difficulties in dissolving the precursors and fabricating uniform and high-quality films have hampered the applications of HDPs for optoelectronic devices. However, this class of compounds is still in its emerging stages, and much effort has been made to apply these materials to PVs (Table 2), photodetectors (Table 3), and light-emitting devices (Table 4).

Solar cells

In 2017, Greul et al. [170] incorporated $Cs_2AgBiBr_6$ into a solar cell for the first time. A device with an optimized $Cs_2AgBiBr_6$ morphology exhibited a PCE of 2.43% with a V_{oc} exceeding 1 V, as depicted in Fig. 9(a). A planar heterojunction solar cell with a high-quality $Cs_2AgBiBr_6$ film was developed by Wu et al. [186] They employed low-pressure-assisted solution processing approach which involved the spin-coating of a precursor solution followed by transferring the films to low-pressure pumping chamber (~20 Pa). Through careful optimization of $Cs_2AgBiBr_6$ films, 1.44% PCE was obtained, yet a hysteresis phenomenon was still observed. Ning et al. [187] also fabricated a planar heterojunction solar cell based on $Cs_2AgBiBr_6$ films. Although a long diffusion length of ~110 nm was observed for photoexcited carriers, the highest PCE was only 1.22%. This low efficiency was attributed to a unsuccessful charge transfer from $Cs_2AgBiBr_6$ to the extraction layers. However, as depicted in Fig. 9(b), the J-V curves in forward and reverse scans exhibited almost no hysteresis. Pantaler et al. [228] also reported hysteresis-free solar cells using $CsAgBiBr_6$. They employed an anti-solvent strategy prior to the annealing step with two types of hole-transporting materials and achieved PCEs of 0.96% and 0.68%, respectively. The absence of hysteresis was ascribed to the reduced trapping and de-trapping of charge carriers and suppressed ion migration.

Very recently, Liu et al. [229] suggested a bandgap engineering strategy to enhance the PCE of $Cs_2AgBiBr_6$-based solar cells. They introduced Sb^{3+} to substitute up to 75% of Bi^{3+} and reduced the optical bandgap by 0.25 eV. The resultant device exhibited an increase in the V_{OC} and PCE by 64 and 31%, respectively, compared to those obtained from the solar cells based on pristine $Cs_2AgBiBr_6$, as depicted in Fig. 9(c). On the other hand, Zhang et al. [225] introduced Rb^+ to substitute the variant fraction of Cs^+ cation in $Cs_2AgBiBr_6$-based solar cells. $(Cs_{1-x}Rb_x)_2AgBiBr_6$ double perovskite exhibited increased absorption at a longer wavelength and decreased defect density. The device performance also increased, as presented in Fig. 9(d), and achieved PCE of

Please cite this article in press as: A. Bibi et al., Materials Today, (2021), https://doi.org/10.1016/j.mattod.2020.11.026

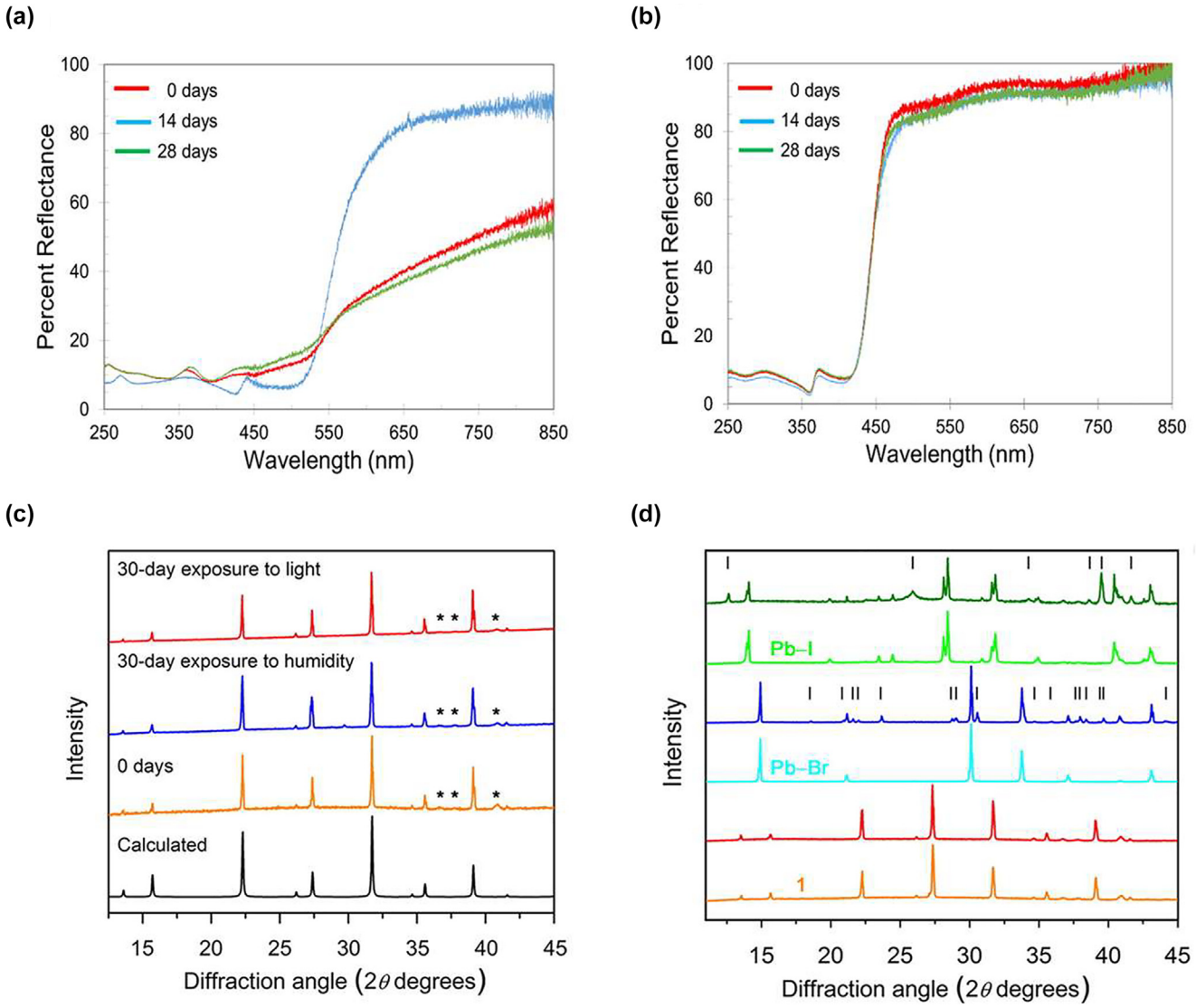

FIGURE 8

(a), (b) UV − Vis diffuse spectra of the light instability of $Cs_2AgBiBr_6$ and $Cs_2AgBiCl_6$ after two and four weeks of light exposure, respectively. Reproduced with permission [132]. Copyright 2016, American Chemical Society. (c) PXRD patterns of 1 after exposure to humidity (55% RH) or light (0.75 Sun). Asterisks denote signals from the sample holder. (d) PXRD patterns of before (orange) and after (red) 72 h at 100 °C, $(MA)PbBr_3$ before (turquoise) and after (blue) 72 h at 60 °C, and $(MA)PbI_3$ before (light green) and after (dark green) 72 h at 60 °C. Vertical bars denote reflections from $PbBr_2$ or PbI_2. Reproduced with permission [144]. Copyright 2016, American Chemical Society.

1.52%, which was 15% higher than that of $Cs_2AgBiBr_6$-based solar cells.

As previously described, high film quality is crucial for the fabrication of high performance perovskite solar cells. Therefore, significant effort has been made to adjust the morphological features of $Cs_2AgBiBr_6$ films [196]. Gao et al. [189] demonstrated an anti-solvent dropping and post-annealing strategy to obtain a high-quality, ultra-smooth $Cs_2AgBiBr_6$ film with high crystallinity. The resulting planar heterojunction solar cell exhibited a PCE of up to 2.23% with no hysteresis. Wang et al. [230] used a sequential vapor deposition approach to fabricate $Cs_2AgBiBr_6$ films. The planar solar cell exhibited an optimized PCE of 1.37% and retained 90% of its PCE value after storage under ambient conditions for 240 h. Igbari et al. [231] compared vacuum-sublimated and solution-processed $Cs_2AgBiBr_6$ and concluded that the solution-processed $Cs_2AgBiBr_6$ exhibited a higher crystallinity, longer photoexcitation lifetime, and higher mobility. With precise control of the composition stoichiometry of solution-processed $Cs_2AgBiBr_6$, they achieved a PCE of 2.51%, as shown in Fig. 9(e), which is the highest value for HDP-based solar cells so far.

In addition to the commonly used $Cs_2AgBiBr_6$, many vacancy-ordered HDPs have also been explored for PV applications due to the direct bandgap. However, poor carrier transport ability and the presence of deep mid-gap defects limited the device performance. Qiu et al. [232] used Cs_2SnI_6 with a bandgap of 1.48 eV as an absorber layer in mesoscopic perovskite solar cells. However, the PCE was around 1%, and low level of PCE was reported in the mixed halide system using $Cs_2SnI_{6-x}Br_x$. The low PCE was attributed to dipole-forbidden transitions from VBM to CBM, resulting in an optical bandgap larger than the fundamental bandgap [139]. As an alternative, Cs_2SnI_6 has been

Please cite this article in press as: A. Bibi et al., Materials Today, (2021), https://doi.org/10.1016/j.mattod.2020.11.026

TABLE 2

Summary of halide double perovskite-based solar cells.

Device structure	PCE %	Stability (days)	References
As hole transport layer			
FTO/c-TiO_2/m-TiO_2/dye with 3D PhC/ **Cs_2SnI_6**/Pt/FTO	7.8	–	[140]
FTO/mutilayered TiO2/Z907 dye/ **Cs_2SnI_6**/Pt	4.23	–	[141]
FTO/c-TiO_2/m-TiO_2/Z907 dye/ **$Cs_2SnI_3Br_3$**/Pt	3.63	–	[142]
As active layer			
ITO/SnO_2/**$Cs_2AgBiBr_6$**/Au	1.44	31	[186]
ITO/SnO_2/**$Cs_2AgBiBr_6$**/P3HT/Au	0.86	31	
ITO/Cu-NiO/**$Cs_2AgBiBr_6$**/C_{60}/BCP/Ag	2.23	10.	[189]
ITO/TiO_2/**$Cs_2AgBiBr_6$**/SpiroOMeTAD/Au	1.22	–	[187]
FTO/c-TiO_2/mTiO_2/**$Cs_2AgBiBr_6$**/PTAA/Au	1.26	–	[228]
FTO/c-TiO_2/m-TiO_2/**$Cs_2AgBiBr_6$**/SpiroOMeTAD/Au	0.9		
FTO/c-TiO_2/m-TiO_2/**$Cs_2AgBiBr_6$**/PCPDTBT/Au	0.68		
FTO/c-TiO_2/mpTiO_2/**$Cs_2AgBiBr_6$**/SpiroOMeTAD/Au	2.5	25	[170]
FTO/c-TiO_2/**$Cs_2AgBiBr_6$**/P3HT/Au	1.37	–	[230]
FTO/c-TiO_2/m-TiO_2/**Cs_2NaBiI_6**/SpiroOMeTAD/Au	0.42	14	[207]
FTO/TiO_2/**Cs_2TiBr_6**/P3HT/Au	2.26	–	[233]
FTO/TiO2/C60/**Cs2TiBr6**/P3HT/Au	3.28	14	
FTO/c-ZnO/mp-ZnO/**Cs_2SnI_6**/P3HT/Ag	0.86	–	[232]
FTO/TiO_2/**Cs_2SnI_6**/P3HT/Ag	0.96	8	[268]
FTO/TiO_2/**Cs_2SnI_6**/P_3HT/Ag	0.47	–	[267]
FTO/c-TiO_2/Sn-TiO_2/**$Cs_2SnI_{6-x}Br_x$**/**Cs_2SnI_6** HTM/LPAH/FTO	2.03	50	[271]

applied as a hole injection layer (HIL) in dye-sensitized solar PV devices due to its lower charge transport resistance than conventional HIL materials. Cs_2TiI_6 thin-films prepared using the low-temperature vapor based method were incorporated into planar heterojunction solar cells by Chen et al. [233], who reported a PCE of 3.3% and superior intrinsic environmental stability.

Photodetector

Visible-UV photodetector

HDPs have been successfully explored for light-detection applications due to their long carrier diffusion lengths, high carrier mobility and more importantly high resistivity. Luo et al. [203] successfully prepared a high-quality single crystal of $Cs_2AgInCl_6$, as depicted in Fig. 10(a). A low dark current (0.01nA), high detectivity ($\sim10^{12}$ Jones), and short response time (0.97 ms) were demonstrated while operating in the UV range. Lei et al. [234] fabricated a $Cs_2AgBiBr_6$ thin-film photodetector using a one-step spin coating process. As depicted in Fig. 10(b), the device exhibited remarkable performance with high responsivity (7.01 AW^{-1}), detectivity ($\sim10^{11}$ Jones), and an external quantum efficiency (EQE) of 2146% along with outstanding operation stability. Yang et al. [235] also fabricated a $Cs_2AgBiBr_6$-based photodetector using an optimized solution process. The optimized solution process exhibited a fast response (17 ns) and high detectivity (3.29×10^{12} Jones). Furthermore, the device retained 94% of its initial photoresponsivity after aged at 150 ℃ for 2300 h.

In contrast, Wu et al. [236] demonstrated a self-powered, highly efficient UV (320–400 nm) and deep blue (435 nm) detector based on $Cs_2AgBiBr_6/SnO_2$ heterojunction, as depicted in Fig. 10(c). Photogenerated carriers in the absorber layer were separated at the interface of $Cs_2AgBiBr_6/SnO_2$ using a built-in field. At 350 nm, high responsivity of 0.1 A W^{-1} and fast response time of 3 ms were reported. A self-powered photodetector based on $Cs_2AgBiBr_6$ films was also reported by Xu et al. [226]. A high detectivity ($\sim10^{13}$ Jones) and responsivity (1.4 AW^{-1}) were obtained owing to efficient charge extraction. More importantly, the device was stable in open air even after three months and could withstand a high temperature of 373 K for 10 h.

X-ray photodetector

Recently, extensive attention has emerged on X-ray detection imaging for medical diagnosis, security screening, and industrial product inspections. HDPs are suitable candidates for X-ray detection due to their desirable properties such as high X-ray attenuation coefficient, defect tolerance, large mobility-lifetime product ($\mu\tau$) and high resistivity. One of the challenges with X-ray photodetectors is the large noise and baseline lift from ionic

TABLE 3

Summary of categories of halide double perovskite-based photodetectors.

Uv-Vis Photo detector.

Material	Responsitivity (AW^{-1})	Detectivity (Jones)	Response Time (ns)	References
$Cs_2AgInCl_6$	–	$\sim10^{12}$	0.97	[203]
$Cs_2AgBiBr_6$	7.01	$\sim10^{11}$	–	[234]
		3.29×10^{12}	17	[235]
	1.46	$\sim10^{13}$	–	[226]
$Cs_2AgBiBr_6/SnO_2$.	0.11	–	3	[236]

X-ray Photo detector

Materials	Approaches	Conditions	Sensitivity ($\mu C\ Gy_{air}^{-1}\ cm^{-2}$)	References
$Cs_2AgBiBr_6$	Ionic Migration	Introduction of BiOBr	250	[237]
		Thermal annealing & Surface Treatment.	105	[238]
	Film Modification	Introduction of Polymer matrix	40	[239]
	Temperature dependent	RT to LN2T	316 at RT. 988 at LN2T	[240]
$(BA)_2CsAgBiBr_7$	Material Insertion	Introduction of $(BA)_2$	4.2	[226]

Please cite this article in press as: A. Bibi et al., Materials Today, (2021), https://doi.org/10.1016/j.mattod.2020.11.026

TABLE 4

Summary of halide double perovskite-based light-emitting materials.

Material	PLQY (%)	Λ_{em} (nm)	References
$Cs_2AgBiCl_6$ (8% OA) NCs	6.7	395	[241]
Cs_2SnCl_6:2.75% Bi NCs	78.9	455	[244]
$Cs_2AgBiBr_6$ NCs	0.7	465	[197]
$Cs_2(Ag_{0.60}Na_{0.40})InCl_6$:0.04% Bi film	86.2 ± 5.0	~550	[246]
$Cs_2AgIn_{0.9}Bi_{0.1}Cl_6$ (8% OA) NCs	36.6	570	[242]
Cs_2AgBiI_6 NCs	<0.1	575	[197]
$Cs_2AgInCl_6$:1% Bi NCs	11.4	580	[245]
$Cs_2Ag_{0.4}Na_{0.6}InCl_6$:Bi NCs	22	620	[243]

migration, which limits detection and imaging performance. Yang et al. [237] reported a novel approach to eliminate ionic migration in $Cs_2AgBiBr_6$ perovskites by introducing BiOBr for heteroepitaxial passivation layers, as depicted in Fig. 11(a). The devices achieved outstanding performance with low noise (1/f noise-free), high sensitivity of 250 μC Gy_{air}^{-1} cm^{-2}, and a spatial resolution of 4.9 lp mm^{-1} for imaging application.

Pan et al. [238] exhibited another approach to eliminate ionic migration through thermal annealing and surface treatment, as depicted in Fig. 11(b). By eliminating the disordering of cations (Ag^+/Bi^{3+}), they reduced the surface trap density and enhanced carrier transport in $Cs_2AgBiBr_6$ single crystals. Employing a simple metal/HDP/metal device configuration, this optimized device exhibited a high sensitivity of 105 μC Gy_{air}^{-1} cm^{-2} and a low detection limit of 59.7n Gy_{air} s^{-1}, suggesting its competitive application for X-ray detection. Li et al. [239] demonstrated $Cs_2AgBiBr_6$ embedded in a polymer matrix using a spin-casting technique. The polymer with hydroxyl functional groups exhibited uniform and large dense films with a sensitivity of 40μC Gy_{air}^{-1} cm^{-2}. Moreover, the addition of polymer matrix led to unique flexible properties exhibiting a 5% tensile/compressive strain without performance degradation, as depicted in Fig. 11(c). Steele et al. [240] provided another photophysical pathway in single-crystal $Cs_2AgBiBr_6$ at both RT and liquid-nitrogen (LN2T) temperatures. This study demonstrated carrier dynamics that influence X-ray sensitivity depending on temperature. The temperature dependence of a single crystal $Cs_2AgBiBr_6$-based device upon cooling ranged from 316 μC Gy_{air}^{-1} cm^{-2} at RT to 988 μC Gy_{air}^{-1} cm^{-2} at LN2T. Moreover, long carrier lifetime of greater than 1.5 μs was demonstrated at 77 K. In contrast, Xu et al. [226] obtained high-quality bulk crystals of $(BA)_2CsAgBiBr_7$ with unique 2D multilayered motifs, which are depicted in Fig. 11(d). The device exhibited a high bulk resistivity and a low density of defects and traps with a decent sensitivity of 4.2 μC Gy_{air}^{-1} cm^{-2}.

Light-emitting materials

Pb-free HDPs with suitable bandgaps also could be used for light-emitting applications. A family of Pb-free silver-bismuth HDPs was intensively studied for use as a light-emitting material owing to its intrinsic chemical stability [211]. Yang et al. [241] synthesized Cs_2AgBiX_6 (X = Cl, Br, I) NCs using the recrystallization method, as depicted in Fig. 12(a). Ligand-passivated NCs presented 100 and 10 times enhanced photoluminescence quantum yields (PLQY) of 6.7% (emission peak: 395 nm) for $Cs_2AgBiCl_6$ and 0.7% (emission peak: 465 nm) for $Cs_2AgBiBr_6$ compared to their ligand-free counterparts. Another silver-bismuth chloride double perovskite with bright orange emission (emission peak: 570 nm) was reported [242], as depicted in Fig. 12(b). By replacing Bi^{3+} with In^{3+} at 75 and 90% ($Cs_2AgIn_xBi_{1-x}Cl_6$ NCs, $x = 0.75$ and 0.9), the maximum PLQY value of 36.6% could be achieved.

Incorporation of Bi^{3+} into HDPs is believed to improve crystallinity and promote exciton localization. Recently, Locardi et al. [243] reported Bi^{3+}-doped NCs with a composition of $Cs_2Ag_{1-x}Na_xInCl_6$ as a candidate for warm white emission, as depicted in Fig. 12(c). A high PLQY up to 22% was achieved from the trapped emission between newly localized states. A Bi^{3+}-doping strategy was also adopted in tin-based and silver-indium-based Pb-free HDPs. Tan et al. [244] synthesized Bi^{3+}-doped Cs_2SnCl_6 for blue emissive phosphors. Consequently, a significant enhancement in the photoluminescence (emission peak: 455 nm, PLQY: 78.9%) was achieved. This is the highest PLQY value ever reported for all-inorganic Pb-free perovskites and is even comparable to the highest value of Pb-based perovskites that emit blue photons. In contrast, Liu et al. [245] optimized the synthetic protocol for Bi^{3+}-doped $Cs_2AgInCl_6$ NCs and achieved a high PLQY of 11.4% (emission peak: 580 nm), largely due to the high crystallinity. More impressively, Luo et al. [246] reported that $Cs_2Ag_{0.60}Na_{0.40}InCl_6$ perovskites doped with 0.04% Bi^{3+} emit warm white light with a PLQY of 86 (±5)%, the highest value ever reported for white-emissive phosphors. Na alloy reduced the electronic dimensionality and broke the parity-forbidden transition, and doping of trace amount of Bi^{3+} suppressed recombination centers, hence simultaneously enhancing the radiative recombination and suppressing the non-radiative recombination, leading to the record PLQY for white phosphors. These materials also exhibited outstanding thermal and working stability, owing to the large exciton binding energy and all-inorganic components. A working electroluminescence device was further built using thermally evaporated $Cs_2Ag_{0.60}Na_{0.40}InCl_6$ film, which suggested the potential application of double halide perovskites for electroluminescence devices.

There are several strategies for tuning the optical bandgap of Pb-free HDPs as shown in Fig. 12(d). For NCs, in particular, halide composition engineering can be utilized as was applied to Pb-based perovskite NCs [241]. However, the limitations of halide segregation under illuminations and external voltage stress of HDP NCs with mixed halide composition need to be explored. Most of HDP light-emitting materials reported to date only contain Cl^- for halide component for the high quantum efficiency and stability [236,242–245]. In addition, Chini et al [247] reported that HDP thin films with mixed halide composition are not only difficult to fabricate, but also their bandgaps do not follow the relative halide composition ratios.

It is also noteworthy that, unlike Pb-based halide perovskites, the bandgap of Pb-free HDP can be modulated by control over the B-site cations through indirect to direct bandgap transition [242]. Moreover, the light-emitting properties of Pb-free HDPs could be tuned by controlling temperature and pressure. Ning et al. [248] modulated the bandgap of $Cs_2AgBiBr_6$ double perovskites using exotic reversible thermochromism. Fang et al. [249] reported 2D HDPs $(BA)_4AgBiBr_8$ that exhibit pressure-induced emission (PIE).

Please cite this article in press as: A. Bibi et al., Materials Today, (2021), https://doi.org/10.1016/j.mattod.2020.11.026

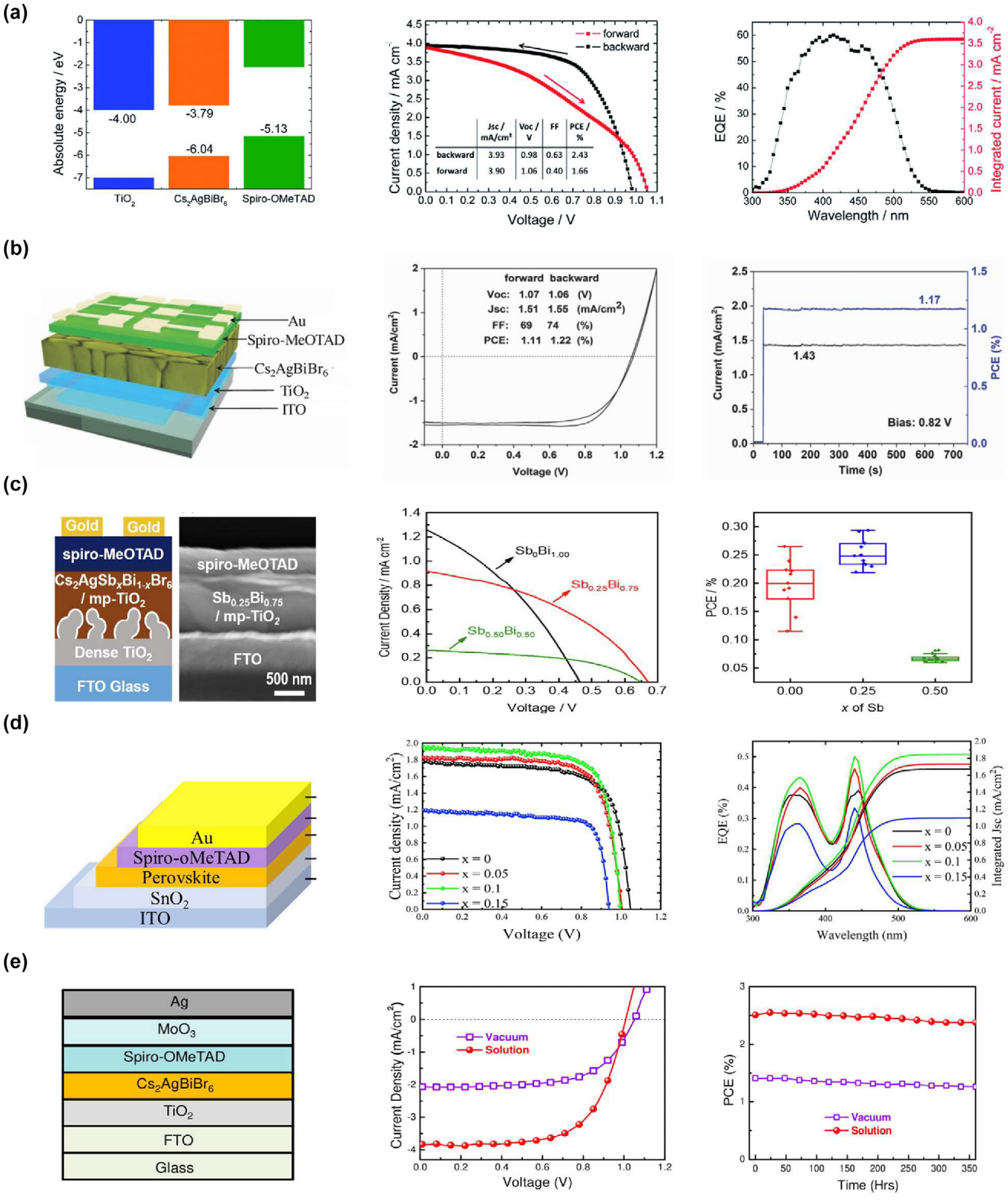

FIGURE 9

Device structure and performance data of HDP-based solar cells. (a) Reproduced with permission [170]. Copyright 2017, Royal Society of Chemistry. (b) Reproduced with permission [187]. Copyright 2018, Wiley-VCH. (c) Reproduced with permission [229]. Copyright 2019, Elsevier. (d) Reproduced with permission [225]. Copyright 2019, Elsevier. (e) Reproduced with permission [231]. Copyright 2019, American Chemical Society.

Please cite this article in press as: A. Bibi et al., Materials Today, (2021), https://doi.org/10.1016/j.mattod.2020.11.026

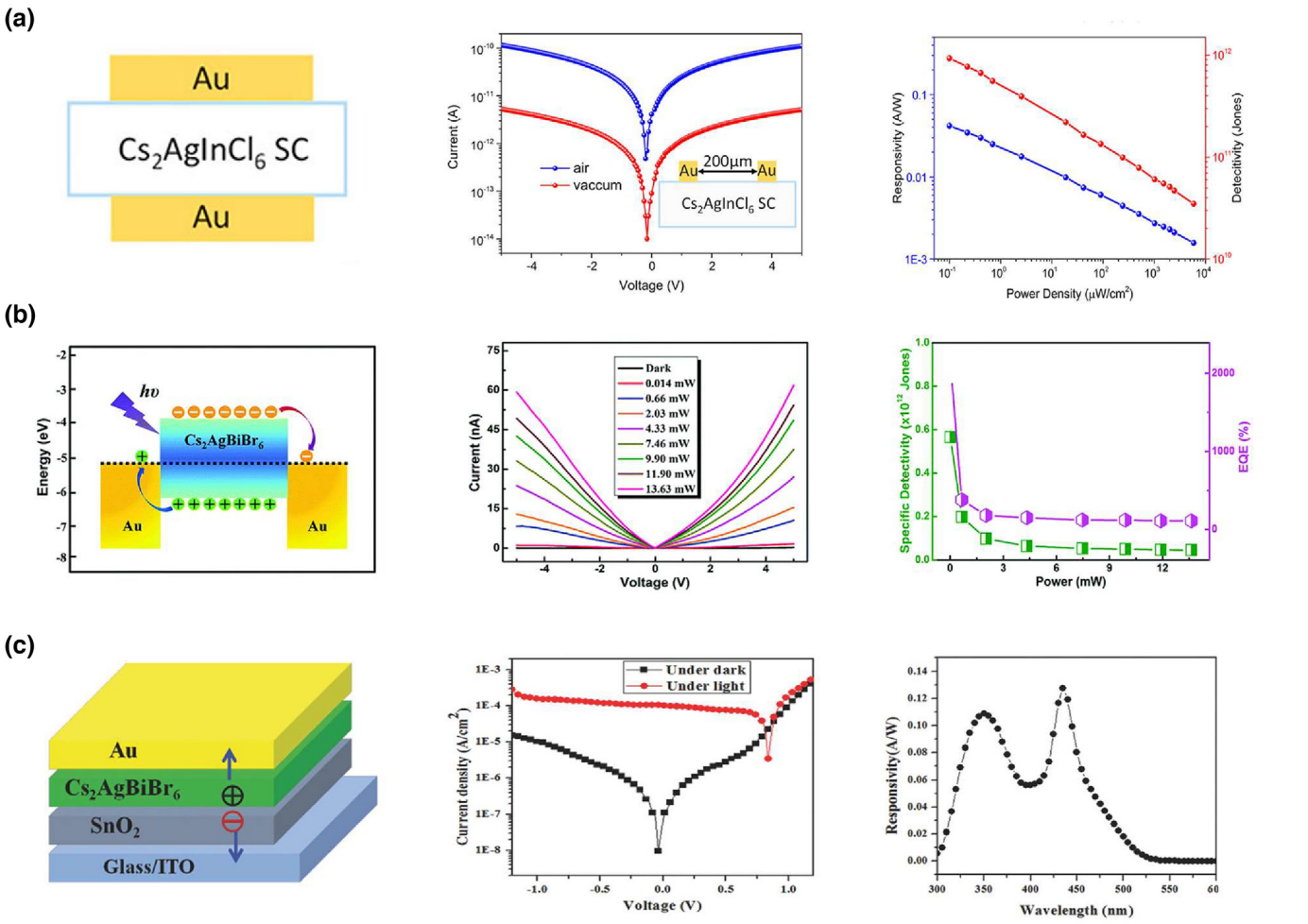

FIGURE 10

Device structure and performance data of HDP-based UV-Vis photodetector devices. (a) Reproduced with permission [203]. Copyright 2017, American Chemical Society. (b) Reproduced with permission [234]. Copyright 2018, Royal Society of Chemistry. (c) Reproduced with permission [226]. Copyright 2018, Wiley-VCH.

Machine learning, simulation, and theoretical studies

First-principles calculations

As the interest in Pb-free HDPs has grown, the number of studies pursuing a fundamental understanding of the structure of optoelectronic properties has increased accordingly [129,132,134,149,166,247,250–256]. Quantum mechanical DFT modeling has been used extensively with various levels of theory to investigate the band structure, thermodynamic stabilities, and mechanical properties of candidate double perovskites as a function of compositional variation. However, the bandgap is normally underestimated from DFT modeling, especially for systems with strong electron correlations [257,258]. Nevertheless, the bandgaps of Pb-based perovskites have been described accurately [190,252,253,259,260], which has been attributed to an error cancellation due to the exclusion of spin orbital coupling effects, which result in an overestimation, and the concurrent underestimation associated with standard DFT [253,254,258,259]. For instance, as reported by Umari and his coworkers [258] for $MAPbI_3$, the bandgap of 1.68 eV calculated using standard DFT agrees closely with the experimental value (1.60 eV). They found that the inclusion of relativistic effects by SOC reduces the bandgap to 0.60 eV, and the addition of many-body perturbation theory based on the single-particle Green function and screened Coulomb interaction (GW) calculation increases the bandgap by ~1 eV [258]. Accordingly, relativistic many-body theory (GW + SOC) can lead to a highly accurate prediction for the bandgap which is good agreement with standard DFT (1.67 eV) [258]. In contrast, the bandgap of $MASnI_3$ was severely underestimated as 0.61 eV using standard DFT while GW + SOC delivered a more accurate bandgap of 1.10 eV [258]. Unfortunately, such calculations are computationally resource-demanding and are not practical for high-throughput investigations.

Another noteworthy study was performed by Volonakis et al. [129], using the PBE0 hybrid functional for a class of pnictogen noble-metal halide perovskites, $Cs_2B^IB^{III}X_6$ (B^I = Cu, Ag, Au, B^{III} = Sb, Bi, and X = Cl, Br, and I), they predicted indirect bandgaps below 2.7 eV as depicted in Fig. 13(a) and (b. Based on this study, the bandgaps are dependent on the size of the halogen and pnictogen rather than the noble metal [129], which is presented in the density of states (DOS) analysis (Fig. 13(c)), in which the VBM and the CBM consist of halogen-p states and

Please cite this article in press as: A. Bibi et al., Materials Today, (2021), https://doi.org/10.1016/j.mattod.2020.11.026

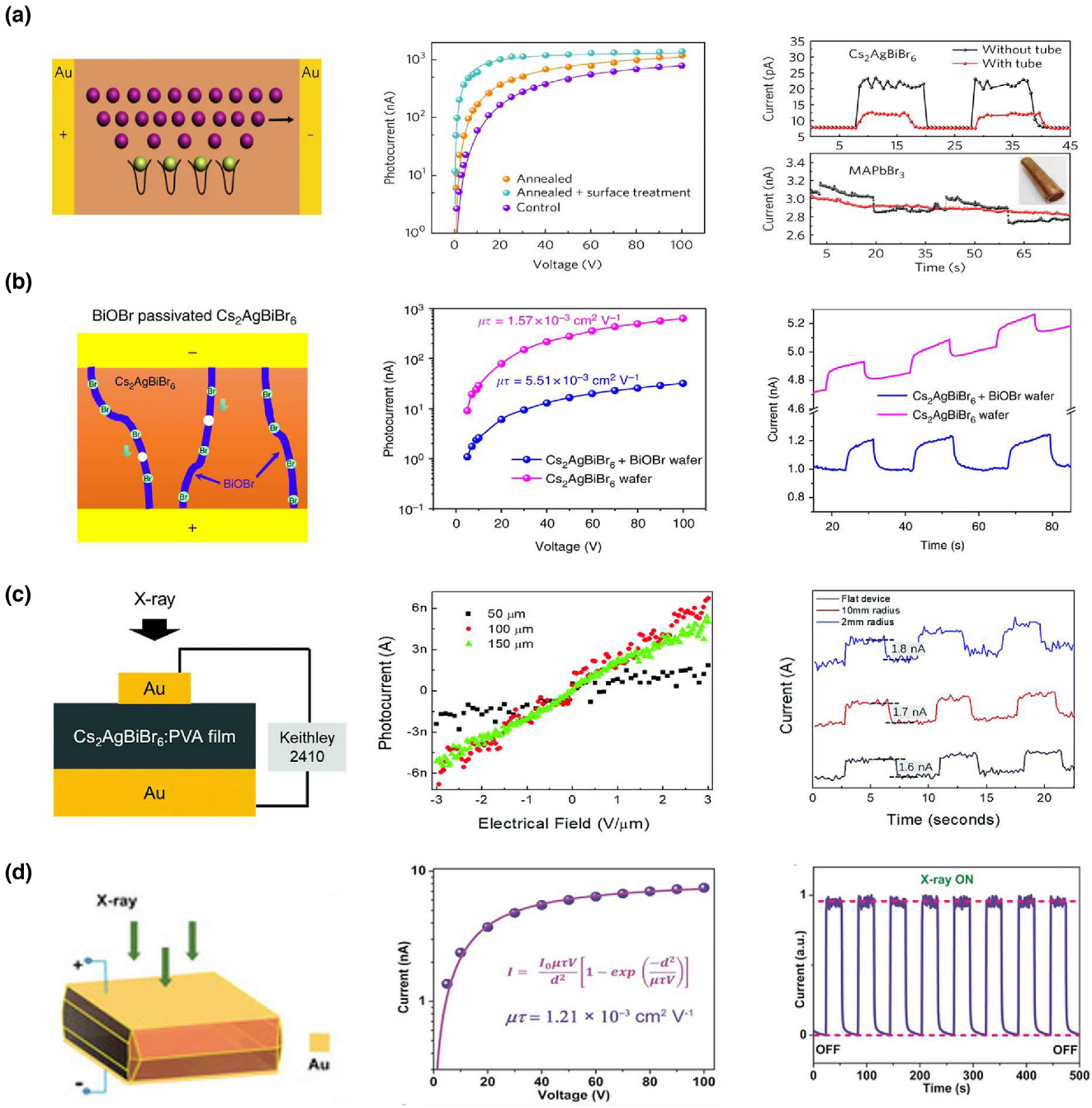

FIGURE 11

Device structure and performance data of HDP-based X-ray photodetector devices. (a) Reproduced with permission [237]. Copyright 2019, American Chemical Society. (b) Reproduced with permission [238]. Copyright 2019, Royal Society of Chemistry. (c) Reproduced with permission [239]. Copyright 2019, Advanced Optical Materials. (d) Reproduced with permission [226]. Copyright 2019, Wiley-VCH.

pnictogen-p states, respectively [129]. From Fig. 13(d), the SOC has a minimal effect on VBM but a more significant effect on the CBM, indicating that the SOC affects the lower conduction bands of heavy-metal-based systems and, consequently, the bandgap of pnictogen noble-metal halide perovskites.

The calculated bandgaps for $Cs_2AgBiCl_6$ and $Cs_2AgBiBr_6$ exhibit discrepancies in literature [129,132,166,247]. As such, Filip et al. [149] used GW + SOC to obtain indirect gaps of 2.4 and 1.8 eV for $Cs_2AgBiCl_6$ and $Cs_2AgBiBr_6$, respectively. These results are in great agreement with experimental band gaps of 2.2 eV for $Cs_2AgBiCl_6$ and 1.9 eV for $Cs_2AgBiBr_6$. Since the allowed direct transitions in this class of material can be over 0.6 eV higher than indirect transitions, this is likely to yield a weaker optical absorption in the visible range. [138,261]. Because the indirect bandgap of the Cs_2AgBiX_6 perovskite family can be attributed to a fundamental mismatch between the symmetry of the s orbitals of Bi and d orbitals of Ag at the band edge, Savory et al. [138] studied the replacement of silver with atoms that contain valence s states, such as In^+ and Tl^+. The inclusions of In^+ and Tl^+ result in direct bandgap transitions. Although the bandgap of Cs_2-

Please cite this article in press as: A. Bibi et al., Materials Today, (2021), https://doi.org/10.1016/j.mattod.2020.11.026

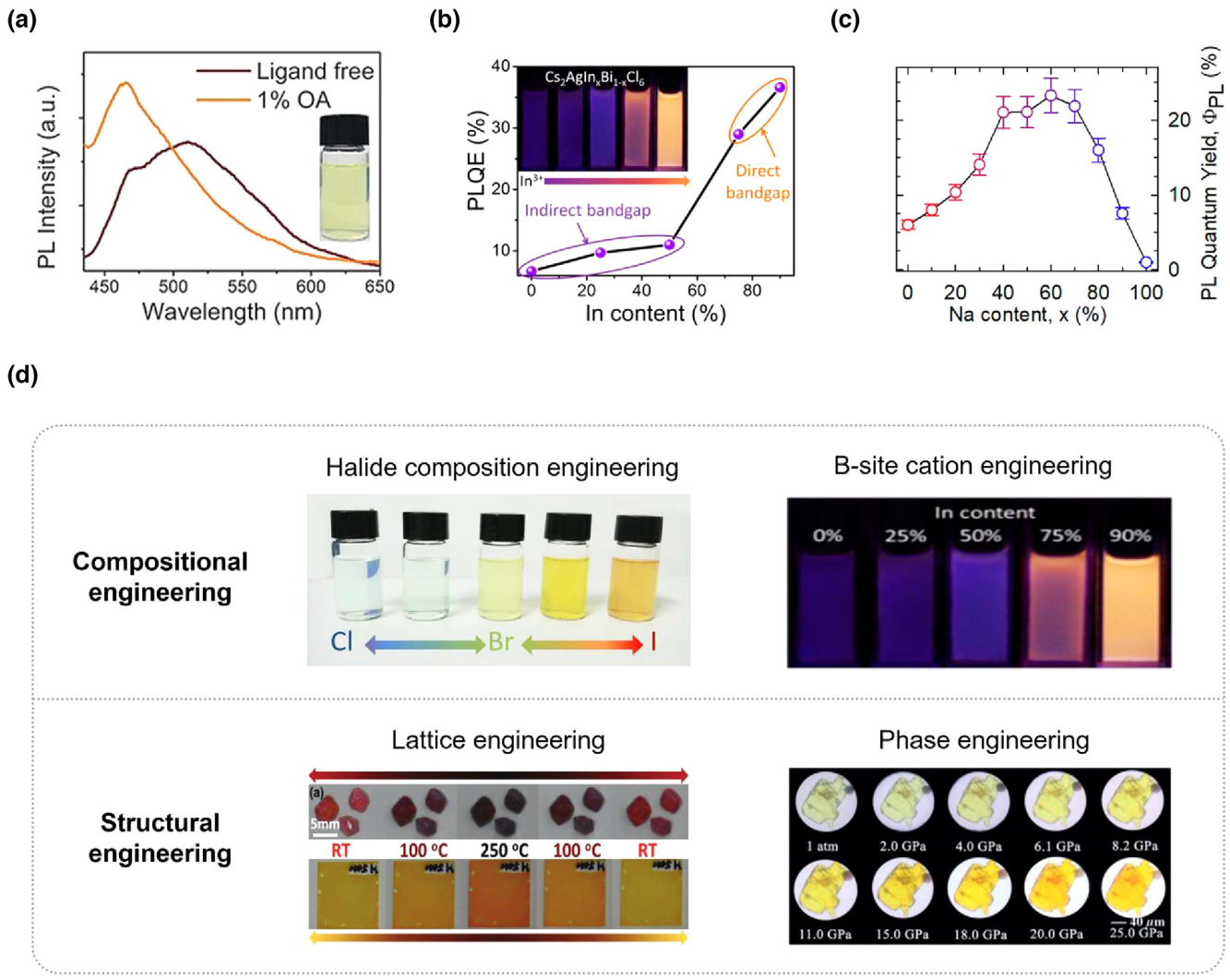

FIGURE 12

(a) Ligand-assisted photoluminescence enhancement of $Cs_2AgBiBr_6$ NCs. Reproduced with permission [241]. Copyright 2018, Wiley-VCH. (b) Substitution of Bi^{3+} with In^{3+} leads to the formation of direct bandgap. Reproduced with permission [242]. Copyright 2018, American Chemical Society. (c) PLQYs of Ag^+ and Bi^{3+}-doped $Cs_2Na_xIn_{1-x}Cl_6$ NCs were modulated by controlling Na content. Reproduced with permission [243]. Copyright 2019, American Chemical Society. (d) Scheme of bandgap tuning strategy in Pb-free HDPs. Reproduced with permission [241]. Copyright 2018, Wiley-VCH. Reproduced with permission [242]. Copyright 2018, American Chemical Society. Reproduced with permission [248]. Copyright 2019, Wiley-VCH. Reproduced with permission [249]. Copyright 2019, Wiley-VCH.

$InBiX_6$ is significantly narrowed ($E_g < 0.5$ eV) [138], $Cs_2TlBiCl_6$ has a direct bandgap of 1.28 eV based on DFT modeling. Thus, if $Cs_2TlBiCl_6$ is thermodynamically stable, it could be highly promising for PV applications.

After the report for $Cs_2TlBiCl_6$ and $Cs_2TlBiBr_6$ [138], Nair et al. [262] predicted that Cs_2TlBiI_6 has a bandgap of 1.37 eV. This result is surprising given that the general trend of the bandgap is to decrease progressing down the halide group. The reason for this unexpected success could be attributed to the different computational methods the researchers used: Savory et al. used HSE06 + SOC for the band structure, whereas Nair et al. used PBE + SOC. Given that band gap can be sensitive to even differences in the amount of exact electron exchange incorporated in HSE06, it is not inconceivable that the discrepancy is due to the different computational schemes. Thus further theoretical investigation is required, potentially using GW methods for this family of compounds.

More recently, Chini et al. [247] investigated the effect of the halide composition in double perovskites on stability and optoelectronic properties. The calculated bandgap of $Cs_2AgBiCl_xBr_{6-x}$ ($x = 0$–6) increases linearly as a function of Cl content when the BiX_6 octahedra contains both Cl^- and Br^- [247], which is expected due to the increased ionicity (electronegativity) of the anion. Interestingly, when the BiX_6 octahedra are composed of only one halide (Cl^- or Br^-), the bandgap is nearly unchanged if the Cl composition remains under 50% [247]. Chini et al. [247] revealed that such structures can benefit from increased ambient stability due to the presence of chloride yet retain the favorable bandgap of $Cs_2AgBiBr_6$.

Pb-based halide perovskites have a key advantage: direct p-p optical transitions [263]. This is due to the lower part of the conduction bands being primarily derived from unoccupied p orbitals of Pb and the upper part of the valence bands being comprised mostly of p orbitals of halide [263]. Thus, in the

Please cite this article in press as: A. Bibi et al., Materials Today, (2021), https://doi.org/10.1016/j.mattod.2020.11.026

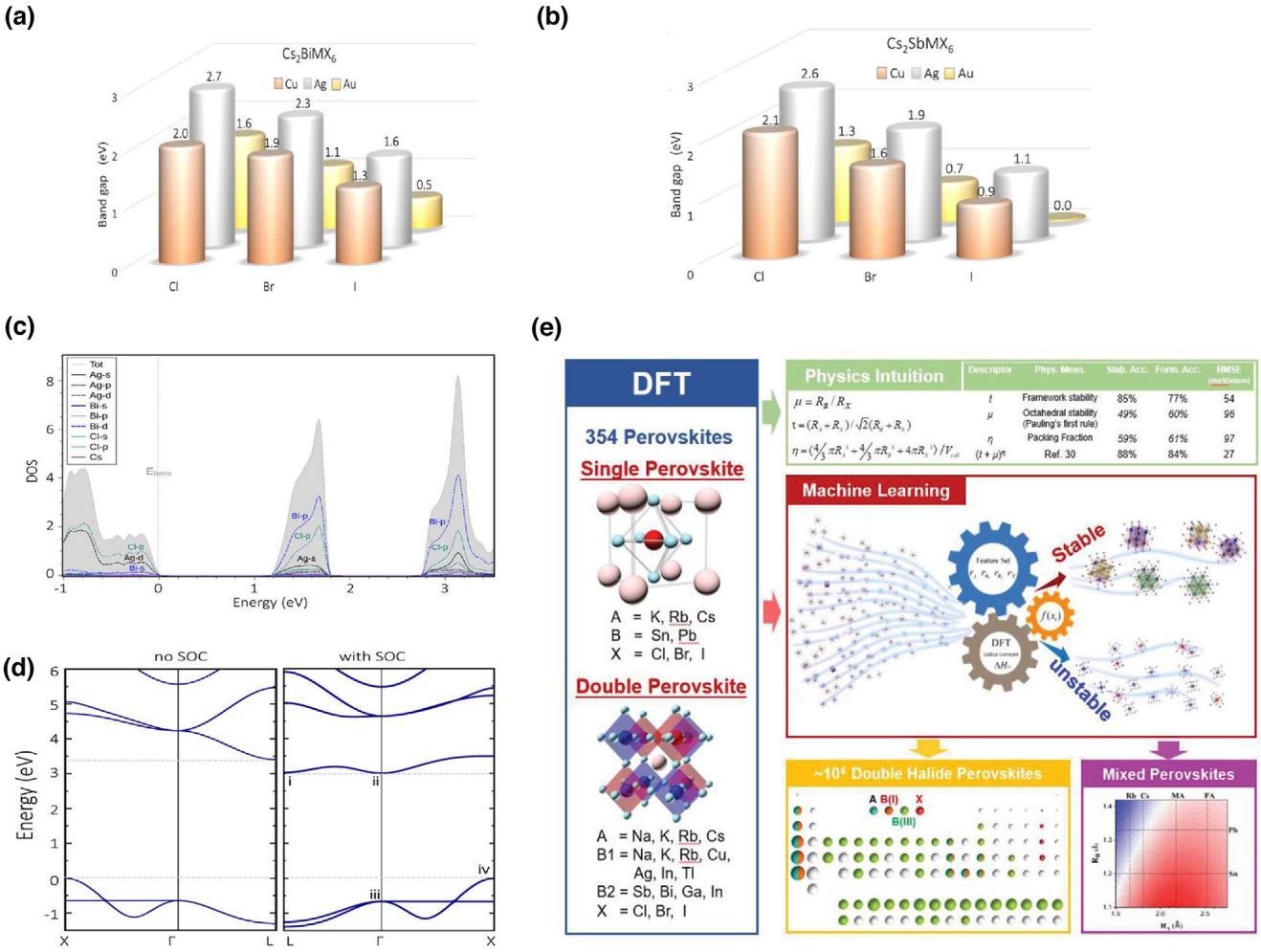

FIGURE 13

Computed indirect electronic bandgaps (PBE0/DFT) of pnictogen noble-metal halide perovskites, $Cs_2B^IB^{III}X_6$ (B^I = Cu, Ag, Au; X = Cl, Br, I) for (a) B^{III} = Bi and (b) B^{III} = Sb. (c) Projected density of states (DOS) of $Cs_2AgBiCl_6$. The valence band top is of Cl-p, Ag-d, and Bi-s characters. The bottom of the conduction band is of Bi-p, Cl-p, and Ag-s characters. (d) Electronic band structure calculated for $Cs_2AgBiCl_6$ without SOC, left, and with SOC, right. Reproduced with permission [129]. Copyright 2016, Wiley-VCH. (e) Schematic illustration of the ML protocol using training data obtained by high-throughput DFT. Reproduction with permission [165]. Copyright 2019, Wiley-VCH.

search for Pb-free perovskites, it is reasonable to investigate isoelectronic cations to Pb^{2+} to retain the desirable electronic structure of Pb-based perovskites [251]. Moreover, the bandgap must be within an appropriate range for single-junction solar cells. One method to control the bandgap is to choose the halide constituent [129]. So far, most experimentally-synthesized double perovskites use Cl^- and Br^-, which yield bandgaps typically too high for single-junction solar cells [129,132,134,149,224,247].

Machine learning

In recent years, experimental and computational advancements have produced a burst of high-throughput studies, which has led to the emergence of a multitude of material databases in diverse fields. In this context, the ML approach has gained significant attention due to its capability for an efficient prediction of various material properties. Consequently, the processes for the discovery and development of new materials with desirable properties are significantly accelerated.

In 2016, Pilania et al. [145] trained a kernel ridge regression (KRR) learning model using DFT-calculated bandgaps of 1306 double perovskites. The original descriptors were composed of simple atomic features such as electronegativities, ionization potentials, electronic energy levels, and valence orbital radii of the constituent atoms. While developing the KRR model, the researchers found that the lowest occupied energy levels of the A-site elements and electronegativities of the B-site elements are the most critical factors determining the bandgap [145], which is somewhat unexpected given that the choice of A-site element has been thought to have a minimal effect on double perovskites [138].

More recently, a data set was built based on all known double perovskites from the literature containing Ca, Sr, and Ba [264]. A random-forest regression (RFR) model was then trained to perform pattern recognition for the developed data set, which pre-

Please cite this article in press as: A. Bibi et al., Materials Today, (2021), https://doi.org/10.1016/j.mattod.2020.11.026

dicted 33 stable double perovskites out of 412 candidates with 3d and 4d/5d transition metal composition [264].

Another ML study [165] was implemented to investigate the thermodynamic stability of double perovskites using the KRR model with the DFT-calculated decomposition energies of 354 candidates (Fig. 13(e)). The descriptors for the KRR model were the ionic radii of the A-, B^{I}-, B^{III}-, and X-sites in an $A_2B^{I}B^{III}X_6$ double perovskite [165]. After training the KRR model, the researchers were able to assess the stability of 246 perovskites that were not present in the training set for the model. That study confirms that the predictive capability of the ML model exceeded that of conventional descriptors such as the Goldschmidt tolerance factor [165].

This summary of the first-principles and ML approaches in the double perovskite field confirms that computational methods can be used to explain fundamental mechanisms and discover promising candidates with targeted optoelectronic and stable thermodynamic properties. Just as computations can complement and explain observed experimental phenomena, it should be stressed to acquire the experimental validation of theoretical findings and techniques. Considering that computational methods provide a useful toolset to guide the design of new double perovskite systems with desirable performance, more effort should be coordinated using experiments to progress toward the successful development of double perovskite-based optoelectronic devices.

Conclusions and outlook

In this study, we presented the most recent developments and possible approaches for the replacement of Pb-based perovskites with halide double perovskite (HDP) materials for related optoelectronic applications. We focused on the motivation behind the demonstrations conducted so far on these compounds. Various material synthetic approaches, smooth film preparation methods, and material characterization techniques are likely significant factors that influence the properties of the resulting materials and the performance of corresponding devices.

A survey of the literature reveals the merits and shortcomings of Pb-free HDPs. However, their photophysical properties and PV performance have not matched the unique properties attained for Pb-based perovskite materials. For a material to illustrate potential as a functional layer in various optoelectronic devices, it must concurrently exhibit all properties that meet the requirements of corresponding applications. A full understanding of these requirements can guide how the materials properties are tailored to meet specific applications.

With their inherent stability and tunable properties, HDPs are promising candidates for practical applications, leading to high-performing, stable, and sustainable optoelectronic devices. X-ray detection is probably one of the most attractive competitive applications for HDPs considering its often large band gap and high crystal quality (enabling low dark current) and indirect transition (harmless to X-ray absorption yet enabling large carrier diffusion length which is imperative for X-ray detection). Although considerable progress has been achieved, many challenges remain including the development of stable compositions with direct bandgaps across the visible range, the improvement of electronic dimensionality and carrier mobility, and the growth of perfect crystals and thin films. Large bandgap (>2 eV) and indirect bandgap are the two key limitations common to HDPs that must be addressed for viable applications. These problems need to be tackled by atomic composition engineering and disordered distribution of B^{+}/B^{3+} cations. The successful realization of halide perovskite compounds that combine the promising photophysical properties of Pb-based perovskites with the unique ambient stability and non-toxicity of HDPs may contribute to a major breakthrough in the field of optoelectronic devices.

From our standpoint, although the new class of HDPs have drawn considerable interest in the past few years for expanding their applications in eco-friendly photovoltaics and optoelectronic devices, still the development of this class of HDPs materials is at its early stages. It is noted that only few members of this family have been studied nd applied so far in optoelectronic applications with a claim of eco-friendly optoelectronic devices, thus paving the route for their commercialization. In addition, the device performance based on this class of HDPs is still far behind than that of conventional Pb-based perovskites, which is currently the major hinderance in their commercialization. New findings for their structural features, morphology control, fundamental photo-physics, tuning of optoelectronic properties, preferred orientation and device optimization are still to be explored to fully exploit the potential of these materials in order to use them as a best possible alternative to Pb-based perovskites.

Declaration of Competing Interest

The authors declare that they have no known competing financial interests or personal relationships that could have appeared to influence the work reported in this paper.

Acknowledgments

This work was supported by National Research Foundation of Korea Grant funded by the Korean Government (NRF-2020R 1A 2C 3003958), the Korea Institute of Energy Technology Evaluation and Planning (KETEP) grant funded by the Korea government (MOTIE) (No. 20173010013340) and Korea Basic Science Institute (National Research Facilities and Equipment Center) grant funded by the Ministry of Education (2020R 1A 6C 101B194). J. Tang acknowledged the financial support by the Major State Basic Research Development Program of China (2016YFB0700702, 2018YFA0703200).

Author contributions

A. Bibi, I. Lee, Y. Nah, and O. Allam contributed equally to this work. A. Bibi and D. H. Kim conceived the concept. A. Bibi prepared the 1st draft. I. Lee, Y. Nah and H. Kim wrote the entire content except for the Section 7. O. Allam and S. S. Jang wrote the Section 7. L. N. Quan, J. Tang, A. Walsh and E. Sargent supervised the overall scope and wrote the manuscript.

References

[1] J. Chen et al., J. Mater. Chem. C 4 (1) (2016) 11–27.
[2] M.M. Lee et al., Science 338 (6107) (2012) 643–647.
[3] S.D. Stranks et al., Science 342 (6156) (2013) 341–344.
[4] G. Xing et al., Science 342 (6156) (2013) 344–347.
[5] H.J. Snaith, J. Phys. Chem. Lett. 4 (21) (2013) 3623–3630.
[6] H.-S. Kim, S.H. Im, N.G. Park, J. Phys. Chem. C 118 (11) (2014) 5615–5625.

Please cite this article in press as: A. Bibi et al., Materials Today, (2021), https://doi.org/10.1016/j.mattod.2020.11.026

[7] G. Hodes, D.J.N.P. Cahen, Nat. Photonics 8 (2) (2014) 87–88.
[8] H.H. Fang et al., Adv. Funct. Mater. 25 (16) (2015) 2378–2385.
[9] T.C. Sum, N.J.E. Mathews, Energy Environ. Sci. 7 (8) (2014) 2518–2534.
[10] X. Wu et al., J. Am. Chem. Soc. 137 (5) (2015) 2089–2096.
[11] J. Sun et al., Adv. Sci. 5 (5) (2018) 1700780.
[12] Marc De Graef, M.E.M., Structure of Materials. An Introduction to Crystallography, Diffraction and Symmetry. Acta Crystallographica Section A. Vol. 68. 2012, Cambridge: Cambridge University Press. 523.
[13] A. Kojima et al., J. Am. Chem. Soc. 131 (17) (2009) 6050–6051.
[14] H.-S. Kim et al., Sci. Rep. 2 (2012) 591.
[15] J.H. Heo et al., Science 8 (5) (2015) 1602–1608.
[16] Y. Zhang et al., Mater. Horiz. 2 (3) (2015) 315–322.
[17] J.H. Noh et al., J. Mater. Chem. A 1 (38) (2013) 11842–11847.
[18] C.-G. Wu et al., Energy Environ. Sci. 8 (9) (2015) 2725–2733.
[19] T. Jiang, W.J.R.A. Fu, RSC Adv. 8 (11) (2018) 5897–5901.
[20] D. Yang et al., Nano Lett. 19 (5) (2019) 3313–3320.
[21] Y. Bai et al., Adv. Funct. Mater. 26 (17) (2016) 2950–2958.
[22] D.-X. Yuan et al., Phys. Chem. Chem. Phys. 17 (40) (2015) 26653–26658.
[23] Z. Gu et al., J. Mater. Chem. A 3 (48) (2015) 24254–24260.
[24] L.-L. Jiang et al., J. Mater. Chem. A 4 (1) (2016) 217–222.
[25] Y. Wang et al., J. Mater. Chem. A 6 (11) (2018) 4860–4867.
[26] J. Min et al., Chem. Mater. 27 (1) (2015) 227–234.
[27] M. Abuhelaiqa et al., Energy Environ. Sci. 12 (6) (2019) 1910–1917.
[28] Y. Hou et al., Adv. Energy Mater. 5 (20) (2015) 1501056.
[29] L. Liu et al., J. Am. Chem. Soc. 137 (5) (2015) 1790–1793.
[30] J.Y. Jeng et al., Adv. Mater. 26 (24) (2014) 4107–4113.
[31] Y. Bai et al., Nat. Commun. 7 (1) (2016) 1–9.
[32] A. Abrusci et al., Nano Lett. 13 (7) (2013) 3124–3128.
[33] O. Malinkiewicz et al., Nat. Photonics 8 (2) (2014) 128–132.
[34] M.R. Filip et al., Nat. Commun. 5 (1) (2014) 1–9.
[35] J.H. Noh et al., Nano Lett. 13 (4) (2013) 1764–1769.
[36] M. Saliba et al., Science 354 (6309) (2016) 206–209.
[37] K. Yao et al., Chem. Mater. 28 (9) (2016) 3131–3138.
[38] D. Luo et al., Adv. Mater. 29 (19) (2017) 1604758.
[39] N.J. Jeon et al., Nature 517 (7535) (2015) 476–480.
[40] N.J. Jeon et al., Nat. Mater. 13 (9) (2014) 897–903.
[41] Z. Liu et al., Adv. Mater. 29 (23) (2017) 1606774.
[42] W. Li et al., J. Am. Chem. Soc. 137 (32) (2015) 10399–10405.
[43] N. Ahn et al., J. Am. Chem. Soc. 137 (27) (2015) 8696–8699.
[44] A. Dualeh et al., Adv. Funct. Mater. 24 (21) (2014) 3250–3258.
[45] F. Zhang et al., Energy Environ. Sci. 11 (12) (2018) 3480–3490.
[46] D. Bi et al., ChemSusChem 10 (7) (2017) 1624–1630.
[47] G.E. Eperon et al., Adv. Funct. Mater. 24 (1) (2014) 151–157.
[48] N. Cheng et al., J. Power Sources 319 (2016) 111–115.
[49] W.S. Yang et al., Science 356 (6345) (2017) 1376–1379.
[50] M. Xiao et al., Angew. Chem. Int. Ed. 53 (37) (2014) 9898–9903.
[51] C.-H. Chiang, Z.-L. Tseng, C.-G. Wu, J. Mater. Chem. A 2 (38) (2014) 15897–15903.
[52] W.S. Yang et al., Science 348 (6240) (2015) 1234–1237.
[53] J. Burschka et al., Nature 499 (7458) (2013) 316–319.
[54] D. Zhao et al., ACS Energy Lett. 3 (2) (2018) 305–306.
[55] N.-G. Park, H.J.A.P. Segawa, ACS Photonics 5 (8) (2018) 2970–2977.
[56] Y. Huang et al., J. Mater. Chem. A 33 (9) (2017) 1730–1751.
[57] Y. Xu et al., Dalton Trans. 48 (11) (2019) 3687–3694.
[58] J. Benick et al., IEEE J. Photovoltaics 7 (5) (2017) 1171–1175.
[59] S. Zhang et al., IEEE J. Photovoltaics 6 (1) (2015) 145–152.
[60] G. Kartopu et al., Solar Energy Materials Solar Cells 191 (2019) 78–82.
[61] D.H. Chun et al., ACS Nano 12 (8) (2018) 8564–8571.
[62] C.A. Perini et al., Semiconductor Sci. Technol. 33 (9) (2018) 094004.
[63] H. Liu et al., J. Mater. Chem. C 5 (25) (2017) 6115–6122.
[64] D. Han et al., APL Mater. 6 (8) (2018) 084902.
[65] H. Wang, D.H. Kim, Chem. Soc. Rev. 46 (17) (2017) 5204–5236.
[66] H. Wang et al., Adv. Opt. Mater. 6 (13) (2018) 1701397.
[67] H. Sun et al., Adv. Mater. 30 (21) (2018) 1706986.
[68] L. Ji et al., Nano Lett. 18 (2) (2018) 994–1000.
[69] H. Cho et al., Science 350 (6265) (2015) 1222–1225.
[70] W. Zou et al., Nat. Commun. 9 (1) (2018) 1–7.
[71] J. Wang et al., Adv. Mater. 27 (14) (2015) 2311–2316.
[72] Z.-K. Tan et al., Nat. Nanotechnol. 9 (9) (2014) 687–692.
[73] D. Bryant et al., Energy Environ. Sci. 9 (5) (2016) 1655–1660.
[74] J.P. Bastos et al., Adv. Energy Mater. 8 (23) (2018) 1800554.
[75] Y. Li et al., J. Phys. Chem. C 121 (7) (2017) 3904–3910.
[76] J.S. Yun et al., Adv. Funct. Mater. 28 (11) (2018) 1705363.
[77] J. Yang et al., ACS Nano 9 (2) (2015) 1955–1963.
[78] M. Salado et al., J. Mater. Chem. A 5 (22) (2017) 10917–10927.
[79] Z. Song et al., In-situ observation of moisture-induced degradation of perovskite solar cells using laser-beam induced current, 2016 IEEE 43rd Photovoltaic Specialists Conference (PVSC), IEEE, 2016.
[80] N. Aristidou et al., Nat. Commun. 8 (1) (2017) 1–10.
[81] A. Senocrate et al., J. Mater. Chem. A 6 (23) (2018) 10847–10855.
[82] B. Conings et al., Adv. Energy Mater. 5 (15) (2015) 1500477.
[83] E.J. Juarez-Perez et al., J. Mater. Chem. A 6 (20) (2018) 9604–9612.
[84] X. Deng et al., J. Mater. Chem. C 4 (38) (2016) 9060–9068.
[85] W. Tress et al., Energy Environ. Sci. 8 (3) (2015) 995–1004.
[86] S. Bae et al., J. Phys. Chem. Lett. 7 (16) (2016) 3091–3096.
[87] A. Babayigit et al., Nat. Mater. 15 (3) (2016) 247.
[88] A. Babayigit et al., Sci. Rep. 6 (1) (2016) 1–11.
[89] M. Kim et al., Energy Environ. Sci. 11 (9) (2018) 2609–2619.
[90] L. Shi et al., ACS Appl. Mater. Interfaces 9 (30) (2017) 25073–25081.
[91] K.C. Tang, P. You, F.J.S.R. Yan, Solar RRL 2 (8) (2018) 1800075.
[92] K. Wang et al., Nat. Commun. 9 (1) (2018) 1–8.
[93] J. Liang et al., J. Am. Chem. Soc. 139 (40) (2017) 14009–14012.
[94] L.A. Frolova et al., J. Mater. Chem. C 7 (18) (2019) 5314–5323.
[95] R. Yang et al., Adv. Mater. 30 (51) (2018) 1804771.
[96] P. Gao, B.M. Yusoff, M.K. Nazeeruddin, Nat. Commun. 9 (1) (2018) 5028.
[97] L.N. Quan et al., J. Am. Chem. Soc. 138 (8) (2016) 2649–2655.
[98] D.H. Cao et al., J. Am. Chem. Soc. 137 (24) (2015) 7843–7850.
[99] C. Ma et al., J. Mater. Chem. A 7 (15) (2019) 8811–8817.
[100] X. Zhang et al., Energy Environ. Sci. 10 (10) (2017) 2095–2102.
[101] Y. Lin et al., ACS Energy Lett. 2 (7) (2017) 1571–1572.
[102] G. Grancini et al., Nat. Commun. 8 (2017) 15684.
[103] P. Li et al., Adv. Mater. 30 (52) (2018) 1805323.
[104] S. Gharibzadeh et al., Adv. Energy Mater. 9 (21) (2019) 1970079.
[105] D. Lin et al., Nano Energy 59 (2019) 619–625.
[106] B. Liu et al., Nano Energy 59 (2019) 715–720.
[107] G. Li et al., Adv. Mater. 28 (18) (2016) 3528–3534.
[108] P.S. Mathew et al., ACS Energy Lett. (2020).
[109] M. Pazoki et al., Phys. Rev. B 93 (14) (2016) 144105.
[110] C.F.J. Lau et al., J. Mater. Chem. A 6 (14) (2018) 5580–5586.
[111] N. Wang et al., Adv. Energy Mater. 6 (24) (2016) 1601130.
[112] S. Shao et al., Adv. Mater. 30 (35) (2018) 1803703.
[113] S. Shao et al., Adv. Energy Mater. 8 (4) (2018) 1702019.
[114] W. Liao et al., Adv. Mater. 28 (42) (2016) 9333–9340.
[115] T.-B. Song et al., J. Am. Chem. Soc. 139 (2) (2017) 836–842.
[116] M. Pazoki, T.J.S.E. Edvinsson, Sustainable Energy Fuels 2 (7) (2018) 1430–1445.
[117] N.K. Noel et al., Energy Environ. Sci. 7 (9) (2014) 3061–3068.
[118] I. Kopacic et al., ACS Appl. Energy Mater. 1 (2) (2018) 343–347.
[119] D. Yang et al., Chem. Mater. 29 (2) (2017) 524–538.
[120] D. Moghe et al., Nano Energy 28 (2016) 469–474.
[121] Z. Li et al., Nat. Commun. 10 (1) (2019) 1027.
[122] P.-P. Sun et al., Nanoscale 8 (3) (2016) 1503–1512.
[123] T. Leijtens et al., ACS Energy Lett. 2 (9) (2017) 2159–2165.
[124] B.W. Park et al., Adv. Mater. 27 (43) (2015) 6806–6813.
[125] A.K. Baranwal et al., Nano Convergence 4 (1) (2017) 26.
[126] P. Harikesh et al., Chem. Mater. 28 (20) (2016) 7496–7504.
[127] Z. Zhang et al., J Phys. Chem. Lett. 8 (17) (2017) 4300–4307.
[128] Z. Xiao et al., Mater. Horiz. 4 (2) (2017) 206–216.
[129] G. Volonakis et al., J Phys Chem Lett 7 (7) (2016) 1254–1259.
[130] V.K. Ravi, N. Singhal, A. Nag, J. Mater. Chem. A 6 (44) (2018) 21666–21675.
[131] N. Chen et al., ACS Appl. Mater. Interfaces (2019).
[132] E.T. McClure et al., Chem. Mater. 28 (5) (2016) 1348–1354.
[133] M. Ghebouli et al., Chin. J. Phys. 56 (1) (2018) 323–330.
[134] G. Volonakis et al., J. Phys. Chem. Lett. 8 (4) (2017) 772–778.
[135] E. Haque, M.A. Hossain, arXiv:.08136, 2018.
[136] Z. Xiao et al., J. Am. Chem. Soc. 139 (17) (2017) 6054–6057.
[137] X.-G. Zhao et al., J. Am. Chem. Soc. 139 (7) (2017) 2630–2638.
[138] C.N. Savory, A. Walsh, D.O. Scanlon, ACS Energy Lett. 1 (5) (2016) 949–955.
[139] A.E. Maughan et al., J. Am. Chem. Soc. 138 (27) (2016) 8453–8464.
[140] B. Lee et al., J. Am. Chem. Soc. 136 (43) (2014) 15379–15385.
[141] A. Kaltzoglou et al., J. Phys. Chem. C 120 (22) (2016) 11777–11785.
[142] A. Kaltzoglou et al., Electrochim. Acta 184 (2015) 466–474.
[143] G. King, P.M. Woodward, J. Mater. Chem. 20 (28) (2010) 5785–5796.
[144] A.H. Slavney et al., J. Am. Chem. Soc. 138 (7) (2016) 2138–2141.
[145] G. Pilania et al., Sci. Rep. 6 (2016) 19375.
[146] W. Wong-Ng et al., Powder Diffr. 29 (4) (2014) 371–378.
[147] M. Vigneshwaran et al., Chem. Mater. 28 (18) (2016) 6436–6440.

Please cite this article in press as: A. Bibi et al., Materials Today, (2021), https://doi.org/10.1016/j.mattod.2020.11.026

[148] O. Lozhkina et al., Chem. Phys. Lett. 694 (2018) 18–22.
[149] M.R. Filip et al., J. Phys. Chem. Lett. 7 (13) (2016) 2579–2585.
[150] Y. Hu et al., Powder Diffr. 25 (S1) (2010) S17–S21.
[151] S. Vasala, M. Karppinen, Prog. Solid State Chem. 43 (1–2) (2015) 1–36.
[152] P. Woodward, R. Hoffmann, A. Sleight, J. Mater. Res. 9 (8) (1994) 2118–2127.
[153] F. Ji et al., Angew. Chem. (2020).
[154] F. Giustino, H.J. Snaith, ACS Energy Lett. 1 (6) (2016) 1233–1240.
[155] C.J. Bartel et al., Sci. Adv. 5 (2) (2019) eaav0693.
[156] P. Cheng et al., New J. Chem. 41 (18) (2017) 9598–9601.
[157] G. Kieslich, S. Sun, A.K. Cheetham, Chem. Sci. 6 (6) (2015) 3430–3433.
[158] Z. Li et al., Chem. Mater. 28 (1) (2015) 284–292.
[159] C. Li et al., Acta Crystallogr. B 64 (6) (2008) 702–707.
[160] J.S. Manser, J.A. Christians, P.V. Kamat, Chem. Rev. 116 (21) (2016) 12956–13008.
[161] Z. Xiao et al., ChemSusChem 9 (18) (2016) 2628–2633.
[162] S. Chakraborty et al., ACS Energy Lett. 2 (4) (2017) 837–845.
[163] M.R. Filip et al., J. Phys. Chem. C 122 (1) (2017) 158–170.
[164] S. Zhao et al., J. Phys. Chem. Solids 117 (2018) 117–121.
[165] Z. Li et al., Adv. Funct. Mater. 29 (9) (2019) 1807280.
[166] N.R. Kumar, R. Radhakrishnan, Mater. Lett. 227 (2018) 289–291.
[167] C.L. Chochos, N. Tagmatarchis, V. Gregoriou, RSC Adv. 3 (20) (2013) 7160–7181.
[168] L. Zhou et al., Small 14 (11) (2018) 1703762.
[169] A. Wang et al., Chem. Mater. 28 (22) (2016) 8132–8140.
[170] E. Greul et al., J. Mater. Chem. A 5 (37) (2017) 19972–19981.
[171] M.H. Rubel et al., Chem. Mater. 28 (2) (2016) 459–465.
[172] S.E. Creutz et al., Nano Lett. 18 (2) (2018) 1118–1123.
[173] J. Zhou et al., J. Mater. Chem. A 6 (5) (2018) 2346–2352.
[174] Y. Bekenstein et al., Nano Lett. 18 (6) (2018) 3502–3508.
[175] J. Zhou et al., J. Mater. Chem. A 5 (29) (2017) 15031–15037.
[176] A. Pan et al., ACS Nano 10 (8) (2016) 7943–7954.
[177] J. De Roo et al., ACS Nano 10 (2) (2016) 2071–2081.
[178] V.K. Ravi et al., J. Phys. Chem. Lett. 8 (20) (2017) 4988–4994.
[179] C.R. Bealing et al., ACS Nano 6 (3) (2012) 2118–2127.
[180] H.-G. Liao et al., Science 345 (6199) (2014) 916–919.
[181] D. Zhang et al., J. Am. Chem. Soc. 137 (29) (2015) 9230–9233.
[182] H. Zhu et al., Nat. Mater. 14 (6) (2015) 636–642.
[183] E. Tiguntseva et al., ACS Nano (2020).
[184] A. Zhizhchenko et al., ACS Nano 13 (4) (2019) 4140–4147.
[185] Q. Zhang et al., ACS Nano 14 (2) (2020) 1577–1585.
[186] C. Wu et al., Adv. Sci. 5 (3) (2018) 1700759.
[187] W. Ning et al., Adv. Mater. 30 (20) (2018) 1706246.
[188] W. Gao et al., ChemPhysChem 19 (14) (2018) 1696–1700.
[189] W. Gao et al., Efficiency. 19 (14) (2018) 1696–1700.
[190] T. Umebayashi et al., Phys. Rev. B 67 (15) (2003) 155405.
[191] E. Mosconi, P. Umari, F. De Angelis, Phys. Chem. Chem. Phys. 18 (39) (2016) 27158–27164.
[192] Y. Fang et al., Nat. Commun. 8 (2017) 14417.
[193] Q. Xu et al., Small Methods 2 (5) (2018) 1700316.
[194] L. Liang, P.J.A.S. Gao, Adv. Sci. 5 (2) (2018) 1700331.
[195] F. Igbari, Z.K. Wang, L.S. Liao, Adv. Energy Mater. 9 (12) (2019) 1803150.
[196] D. Bartesaghi et al., J. Phys. Chem. C 122 (9) (2018) 4809–4816.
[197] P. Zhang, J. Yang, S.-H. Wei, J. Mater. Chem. A 6 (4) (2018) 1809–1815.
[198] Q. Li et al., Angew. Chem. 56 (2017) 15969–15973.
[199] A.H. Slavney et al., J. Am. Chem. Soc. 139 (14) (2017) 5015–5018.
[200] K.Z. Du et al., Angew. Chem. Int. Ed. 56 (28) (2017) 8158–8162.
[201] T.T. Tran et al., Mater. Horiz. 4 (4) (2017) 688–693.
[202] Z. Xiao et al., Angew. Chem. 129 (40) (2017) 12275–12279.
[203] J. Luo et al., ACS Photonics 5 (2) (2018) 398–405.
[204] A. Nag, Chem. Commun. 54 (41) (2018) 5205–5208.
[205] J. Xu et al., J. Phys. Chem. Lett. 8 (18) (2017) 4391–4396.
[206] T. Li et al., Phys. Rev. Appl 10 (4) (2018) 041001.
[207] C. Zhang et al., Sustainable Energy Fuels 2 (11) (2018) 2419–2428.
[208] G. Tang et al., J. Phys. Chem. Lett. 9 (1) (2018) 43–48.
[209] B.A. Connor et al., J. Am. Chem. Soc. 140 (15) (2018) 5235–5240.
[210] A.S. Kshirsagar, A. Nag, J. Chem. Phys. 151 (16) (2019) 161101.
[211] J.C. Dahl et al., Chem. Mater. 31 (9) (2019) 3134–3143.
[212] F. Rissner et al., Org. Electron. 13 (12) (2012) 3165–3176.
[213] A. Lamichhane, N.M.J.M. Ravindra, Materials 13 (8) (2020) 1917.
[214] N. Ravindra et al., Infrared Phys. Technol. 50 (1) (2007) 21–29.
[215] S.J. Tripathy, Opt. Mater. 46 (2015) 240–246.
[216] P.R.J.N. Varadwaj, Nanomaterials 10 (5) (2020) 973.
[217] G. Zheng et al., Nat. Commun. 9 (1) (2018) 1–11.
[218] L. Cinà, et al., Investigating thermoelectric properties of lead-halide perovskites fabricated with large area techniques, in 2015 IEEE 15th International Conference on Nanotechnology (IEEE-NANO). 2015: Rome.
[219] T. Krishnamoorthy et al., J. Mater. Chem. A 3 (47) (2015) 23829–23832.
[220] M.T. Klug et al., Energy Environ. Sci. 10 (1) (2017) 236–246.
[221] J. Jin et al., ACS Appl. Mater. Interfaces 9 (49) (2017) 42875–42882.
[222] Y.-J. Li et al., RSC Adv. 7 (56) (2017) 35175–35180.
[223] L. Dong et al., Comput. Mater. Sci. 141 (2018) 49–58.
[224] F. Wei et al., Chem. Mater. 29 (3) (2017) 1089–1094.
[225] Y. Zhang et al., Chem. Mater. 31 (19) (2019) 7962–7969.
[226] Z. Xu et al., Angew. Chem. Int. Ed. 58 (44) (2019) 15757–15761.
[227] F. Wei et al., Mater. Horiz. 3 (4) (2016) 328–332.
[228] M. Pantaler et al., ACS Energy Lett. 3 (8) (2018) 1781–1786.
[229] Y. Liu et al., Mater. Today 28 (2019) 25–30.
[230] M. Wang et al., Solar RRL 2 (12) (2018) 1800217.
[231] F. Igbari et al., Nano Lett. 19 (3) (2019) 2066–2073.
[232] X. Qiu et al., Phys. Status Solidi –Rapid Res. Lett. 10 (8) (2016) 587–591.
[233] M. Chen et al., Joule 2 (3) (2018) 558–570.
[234] L.-Z. Lei et al., J. Mater. Chem. C 6 (30) (2018) 7982–7988.
[235] J. Yang et al., Adv. Opt. Mater. 7 (13) (2019) 1801732.
[236] C. Wu et al., Adv. Opt. Mater. 6 (22) (2018) 1800811.
[237] B. Yang et al., Nat. Commun. 10 (1) (2019) 1–10.
[238] W. Pan et al., Nat. Photonics 11 (11) (2017) 726–732.
[239] H. Li et al., J. Mater. Chem. C 6 (44) (2018) 11961–11967.
[240] J.A. Steele et al., Adv. Mater. 30 (46) (2018) 1804450.
[241] B. Yang et al., Angew. Chem. 130 (19) (2018) 5457–5461.
[242] B. Yang et al., J. Am. Chem. Soc. 140 (49) (2018) 17001–17006.
[243] F. Locardi et al., ACS Energy Lett. 4 (8) (2019) 1976–1982.
[244] Z. Tan et al., Adv. Funct. Mater. 28 (29) (2018) 1801131.
[245] Y. Liu et al., Chem. Mater. 31 (9) (2019) 3333–3339.
[246] J. Luo et al., Nature 563 (7732) (2018) 541–545.
[247] M.K. Chini et al., Chem. Phys. 529 (2020) 110547.
[248] W. Ning et al., Adv. Funct. Mater. 29 (10) (2019) 1807375.
[249] Y. Fang et al., Angew. Chem. 131 (43) (2019) 15393–15397.
[250] S.A. Dar, V. Srivastava, U.K. Sakalle, Comput. Condens. Matter 18 (2019) e00351.
[251] M.K. Jana et al., J. Am. Chem. Soc. 141 (19) (2019) 7955–7964.
[252] F. Li et al., APL Mater. 6 (11) (2018) 114203.
[253] E. Mosconi et al., J. Phys. Chem. C 117 (27) (2013) 13902–13913.
[254] Z. Xiao, Y. Yan, Adv. Energy Mater. 7 (22) (2017) 1701136.
[255] P.-K. Kung et al., Solar RRL 4 (2) (2020) 1900306.
[256] H. Yin et al., Solar RRL 3 (9) (2019) 1900148.
[257] J. Even et al., J. Phys. Chem. Lett. 4 (17) (2013) 2999–3005.
[258] P. Umari, E. Mosconi, F. De Angelis, Sci. Rep. 4 (2014) 4467.
[259] N.-G. Park et al., Unconventional Thin Film Photovoltaics, Royal Society of Chemistry, 2016.
[260] Y. Chang, C.H. Park, K. Matsuishi, J.-Korean Phys. Soc. 44 (2004) 889–893.
[261] L. Yu et al., Adv. Energy Mater. 3 (1) (2013) 43–48.
[262] S. Nair et al., J. Phys.: Condens. Matter 31 (44) (2019) 445902.
[263] W.J. Yin, T. Shi, Y.J.A.M. Yan, Adv. Mater. 26 (27) (2014) 4653–4658.
[264] A. Halder, A. Ghosh, T.S. Dasgupta, Phys. Rev. Mater. 3 (8) (2019) 084418.
[265] R. Hoye et al., Adv. Mater. Interfaces (2018).
[266] B. Vargas et al., J. Am. Chem. Soc. 139 (27) (2017) 9116–9119.
[267] Y. Jiang et al., Mater. Lett. 199 (2017) 50–52.
[268] X. Qiu et al., Solar Cells 159 (2017) 227–234.
[269] A.E. Maughan et al., Chem. Mater. 30 (11) (2018) 3909–3919.
[270] Z. Deng et al., J. Mater. Chem. A 4 (31) (2016) 12025–12029.
[271] B. Lee et al., Sustainable Energy Fuels 1 (4) (2017) 710–724.

Please cite this article in press as: A. Bibi et al., Materials Today, (2021), https://doi.org/10.1016/j.mattod.2020.11.026